AFRL-RX-WP-TR-2010-4088

COLLABORATIVE RESEARCH AND DEVELOPMENT (CR&D)

Delivery Order 0051: Atomic Scale Transmission Electron Microscope Image Modeling and Application to Semiconductor Heterointerface Characterization

Krishnamurthy Mahalingam

Universal Technology Corporation

JANUARY 2008
Final Report

AIR FORCE RESEARCH LABORATORY
MATERIALS AND MANUFACTURING DIRECTORATE
WRIGHT-PATTERSON AIR FORCE BASE, OH 45433-7750
AIR FORCE MATERIEL COMMAND
UNITED STATES AIR FORCE

NOTICE AND SIGNATURE PAGE

Using Government drawings, specifications, or other data included in this document for any purpose other than Government procurement does not in any way obligate the U.S. Government. The fact that the Government formulated or supplied the drawings, specifications, or other data does not license the holder or any other person or corporation; or convey any rights or permission to manufacture, use, or sell any patented invention that may relate to them.

This report was cleared for public release by the USAF 88th Air Base Wing (88 ABW) Public Affairs Office (PAO) and is available to the general public, including foreign nationals. Copies may be obtained from the Defense Technical Information Center (DTIC) (http://www.dtic.mil).

AFRL-RX-WP-TR-2010-4088 HAS BEEN REVIEWED AND IS APPROVED FOR PUBLICATION IN ACCORDANCE WITH THE ASSIGNED DISTRIBUTION STATEMENT.

*//Signature//	//Signature//
MARK N. GROFF Project Engineer Business Operations Branch Integration and Operations Division	KENNETH A. FEESER Chief Business Operations Branch Integration and Operations Division

This report is published in the interest of scientific and technical information exchange, and its publication does not constitute the Government's approval or disapproval of its ideas or findings.

*Disseminated copies will show "//Signature//" stamped or typed above the signature blocks.

REPORT DOCUMENTATION PAGE

Form Approved
OMB No. 0704-0188

1. REPORT DATE *(DD-MM-YY)*	2. REPORT TYPE	3. DATES COVERED *(From - To)*
January 2008	Final	19 May 2006 – 31 January 2008

4. TITLE AND SUBTITLE
COLLABORATIVE RESEARCH AND DEVELOPMENT (CR&D)
Delivery Order 0051: Atomic Scale Transmission Electron Microscope Image Modeling and Application to Semiconductor Heterointerface Characterization

5a. CONTRACT NUMBER
F33615-03-D-5801-0051

5b. GRANT NUMBER

5c. PROGRAM ELEMENT NUMBER
62102F

6. AUTHOR(S)
Krishnamurthy Mahalingam

5d. PROJECT NUMBER
4349

5e. TASK NUMBER
L0

5f. WORK UNIT NUMBER
4349L0VT

7. PERFORMING ORGANIZATION NAME(S) AND ADDRESS(ES)
Universal Technology Corporation
1270 North Fairfield Road
Dayton, OH 45432-2600

8. PERFORMING ORGANIZATION REPORT NUMBER
S-531-051

9. SPONSORING/MONITORING AGENCY NAME(S) AND ADDRESS(ES)
Air Force Research Laboratory
Materials and Manufacturing Directorate
Wright-Patterson Air Force Base, OH 45433-7750
Air Force Materiel Command
United States Air Force

10. SPONSORING/MONITORING AGENCY ACRONYM(S)
AFRL/RXOB

11. SPONSORING/MONITORING AGENCY REPORT NUMBER(S)
AFRL-RX-WP-TR-2010-4088

12. DISTRIBUTION/AVAILABILITY STATEMENT
Approved for public release; distribution unlimited.

13. SUPPLEMENTARY NOTES
PAO Case Number: 88ABW 2009-0039; Clearance Date: 01 Feb 2009.

14. ABSTRACT
This research in support of the Air Force Research Laboratory Materials and Manufacturing Directorate was conducted from 19 May 2006 through 31 January 2008. This task developed and used computer models of electron beam transmission through complex semiconductor heterostructures to determine the interface compositions in real images, and to study how growth and/or processing conditions affect the layers and interfaces. The techniques and models developed, as well as the results of applications of these models to AFRL/MLPS-provided semiconductor samples are reported.

15. SUBJECT TERMS

16. SECURITY CLASSIFICATION OF:			17. LIMITATION OF ABSTRACT:	18. NUMBER OF PAGES	19a. NAME OF RESPONSIBLE PERSON (Monitor)
a. REPORT	b. ABSTRACT	c. THIS PAGE			Mark N. Groff
Unclassified	Unclassified	Unclassified	SAR	50	19b. TELEPHONE NUMBER *(Include Area Code)* N/A

Standard Form 298 (Rev. 8-98)
Prescribed by ANSI Std. Z39-18

Table of Contents

List of Figures

SUMMARY

In this report we describe results from transmission electron microscope (TEM) studies on a variety of III-V semiconductor thin films grown by molecular beam epitaxy (MBE). The various techniques employed in these studies include, conventional bright and dark-field imaging, and phase retrieval high-resolution transmission electron microscopy. The material systems investigated include, InAs/GaSb superlattices and a variety of other multilayered thin films involving multilayered quantum-dot infrared photodetectors (QDIP), quantum cascade laser structures and quantum-well infrared photodetectors. The important results from each of these studies may be summarized as follows:

An approach we had previously developed for atomic-scale compositional analysis of quaternary III-V semiconductor interfaces was used to investigate the role of interface tailoring in optimizing the properties of InAs/GaSb superlattices.

Our results showed that untailored interfaces exhibit significant compositional grading in both In-Ga and As-Sb sublattices

Interface tailoring leads to significant improvement in compositional abruptness, especially at the GaSb-on-InAs interface.

This improvement is essential to preserve the intended InAs layer thickness and therby achieve desired properties.

A detailed analysis of InGaAs QDIP structures showed that multiple QD-layers with up to 20 stacks could be achieved with low dislocation densities. However, we observe that the nucleation and propagation of dislocation is possible during growth of the top GaAs-contact layer.

1.0 INTRODUCTION

Artificially layered III-V structures grown by epitaxial techniques such as molecular beam epitaxy (MBE) and metal organic chemical vapor deposition (MOCVD) are important materials for optoelectronic applications. Examples of such materials include AlGaAs/GaAs and InGaAs/GaAs heterostructures, used in high electron mobility transistors [1] and lasers [2]. More recently, heterostructures containing combinations of arsenides and antimonides are of interest for number applications, including long-wavelength infrared detectors [3], infrared lasers [4], field effect transistors [5], resonant tunneling diodes [6]. Materials for many of these applications involve extremely thin layers requiring precise control of both thickness and composition of the constituent layers. From a microstructural perspective the important factors which determine high-quality material include layer thickness, interface abruptness, layer composition, and the composition modulation within each layer (as in graded $Al_xGa_{(1-x)}As$ layers for photo refractive applications). In addition, structural defects, such as dislocations and stacking faults, arising from factors related to growth conditions or strain relaxation also play a critical role in the application of these materials.

The past two decades have witnessed significant developments in the application of transmission electron microscopy (TEM) for the routine analysis of III-V semiconductor heterostructures. In particular, high-resolution techniques have been developed to characterize III-V heterostructure interfaces at the atomic level [7-11]. In this study we apply cross-sectional TEM techniques, involving conventional bright-field and dark-field imaging, high-resolution TEM (HRTEM) and analytical electron microscopy (AEM), to characterize a variety of III-V semiconductor thin films. The materials investigated include superlattices based on the InAs-GaSb system and novel self-assembled quantum dot structures, all of which were grown by MBE. Furthermore, a new approach to quantifying the stoichiometry interfaces at atomic resolution is also developed.

2.0 EXPERIMENTAL PROCEDURE

The theoretical concepts underlying the application of TEM for imaging of III-V semiconductor systems have been described in detail in the earlier reports [12, 13]. Briefly, we use the (200) dark-field imaging condition to maximize image contrast arising from the individual layers in the superlattice /heterostructure. The two-beam bright-field imaging condition with the diffraction vector (denoted **g**) along <200> and <220> are used to image defects in the structure. The procedure for obtaining these imaging conditions are described in standard text books on transmission electron microscopy [14]. For the sake of continuity the procedures for performing the HRTEM experiments are described in Chapter 3.2, along with methods employed for performing the data analysis.

Samples for TEM observations was performed by Ar^+ ion-milling at 5 keV with liquid nitrogen cooling until perforation and subsequent cleaning at 3 keV to minimize the thickness of the amorphous surface layer induced by the milling process. In the XEDS experiments samples were also prepared by the small angle cleavage technique. TEM observations were performed using a Philips-CM 200 FEG transmission electron microscope equipped with a field emission gun, operated at an accelerating voltage of 200 kV.

3.0 RESULTS AND DISCUSSION

3.1 Chemical Mapping of Interfaces in InAs/GaSb Superlattices

Heterostructures derived from the InAs-GaSb system are promising materials for a variety of next generation optoelectronic devices, such as mid-infrared lasers and tunable long-wavelength detectors (3-6). The versatility of these heterostructures is based on the principle that their electronic and optical properties can be tuned by appropriately designing the thickness and composition of the individual layers. However, control of interface stoichiometry is crucial to realizing structures with desired properties. Interfaces are known to play a unique role in these materials due to the distinctly different types of interfacial bonds obtainable depending on growth conditions (for instance the interfaces in InAs-GaSb heterostructures can be "InSb-like" or "GaAs-like"). Considerable attention is now focused on tailoring interface stoichiometry to optimize properties. A key requirement in this endeavor is the ability to accurately quantify the composition of interfaces (typically < 1 nm in width). Although several techniques based on high-resolution transmission electron microscopy (HRTEM) have been developed since the early 1990's [7-11], these are applicable only to ternary systems (such as those based on the AlAs-GaAs and InAs-GaAs systems).

In a previous study we have developed a method for atomic scale compositional analysis of quaternary III-V semiconductor interfaces with mixing in both cation and anion sublattices (15,16). Our approach utilizes the principles of phase retrieval HRTEM based on the focal series reconstruction technique, used in combination with multivariate statistical analysis for quantitative image analysis. In the present study we have applied this approach to investigate the role of interface engineering in optimizing properties of InAs/GaSb superlattices. Specifically, we present results from two structures: one in which the alternating InAs and GaSb layers are grown with no interface control and the other in which each interface is tailored to be "InSb-like," wherein a controlled deposition of 0.8 ML (0.26 nm) of InSb precedes the growth of each InAs/GaSb layer. Figure 1 shows the (200) dark-field images of the structures examined where Figure 1 (a) corresponds to the superlattice structure in which the individual layers were grown with no interface control and Figure 1 (b) the structure in which the interfaces were engineered to InSb-like. These nominal thicknesses of the InAs (dark) and the GaSb (bright) layers in both structures were 4.9 nm and 4.4 nm, respectively, and were designed for photodetectors with cut-off wavelength at 10 μm.

The interfaces in Figures 1 (a) and (b) were imaged along the [001] zone axis to ensure adequate separation between the cation and anion sublattices. Cross-sectional samples were prepared by mechanical grinding followed by ion-milling to perforation at an accelerating voltage of 5kV. To reduce milling induced surface roughness further milling was performed at 3kV, which was then followed by final polishing at 1kV. The entire milling process was performed with the samples mounted on a liquid-N_2 cooled cryostage. The HRTEM observations were performed using the Philips CM300 FEG/UT TEM located at the National Center for Electron Microscopy, Berkeley, CA. A detail report describing the experimental set-up to perform the FSR technique using this TEM has been published previously (17,18). Briefly, a through focus series of 20 HRTEM images was digitally acquired at equally spaced defocus values, starting at an underfocus value of -270 nm and a focal increment step of 2 nm. The images were recorded using a 2048x2048 slow-scan charge-coupled device (CCD) camera with a Gatan Image Filter (GIF) attachment at a spatial sampling rate of 0.02 nm/pixel. Based on detailed image simulations we estimate the thickness of the regions examined to be in the range of 4-6 nm.

The numerical EPWF reconstruction procedure was performed using TrueImage software (19), a commercial version of the Philips/Brite-Euram focal series reconstruction software package developed by Thust and Coene (20,21), which also includes a module for correcting residual aberrations. Prior to reconstruction, a noise reduction procedure employing the background subtraction filter (22) was applied to the digitally acquired HRTEM images to reduce contributions from the amorphous layers on the top and bottom surfaces of the sample.

Figure 2 (a) shows the reconstructed phase image of the superlattice with no interface control wherein, the atomic sites with stronger (weaker) phase maxima correspond to the In (As) sublattice within InAs layer, and the Sb (In-Ga) sublattice within InGaSb layer. The arrows in denote the interfacial regions corresponding to those exhibiting dark contrast in Figure 1 (a), indicating that these regions are about 7 atomic layers (approx. 1 nm) in width. A close inspection of the atomic sites within these regions reveals a systematic change in their respective phase maxima. This is easily recognized in the line scans across interfaces along adjacent In-Ga (denoted by line “a-b”) and As-Sb sublattices (denoted by line “c-d”), shown in Figures 2(b) and 2(c), respectively, where an asymmetry in grading at the interfacial regions is exhibited in both sublattices. Figure 3 shows the corresponding observations for the superlattice structure grown with interface control, where the reconstructed phase image is shown in Figure 3 (a) and the

phase profiles along the As-Sb and In-Ga sublattices are shown in Figures 3 (b) and (c) respectively. The width of each interface in this sample appears to be around 4 atomic layers (0.6 nm), indicating they are more abrupt in comparison to those observed Figure 2 (a).

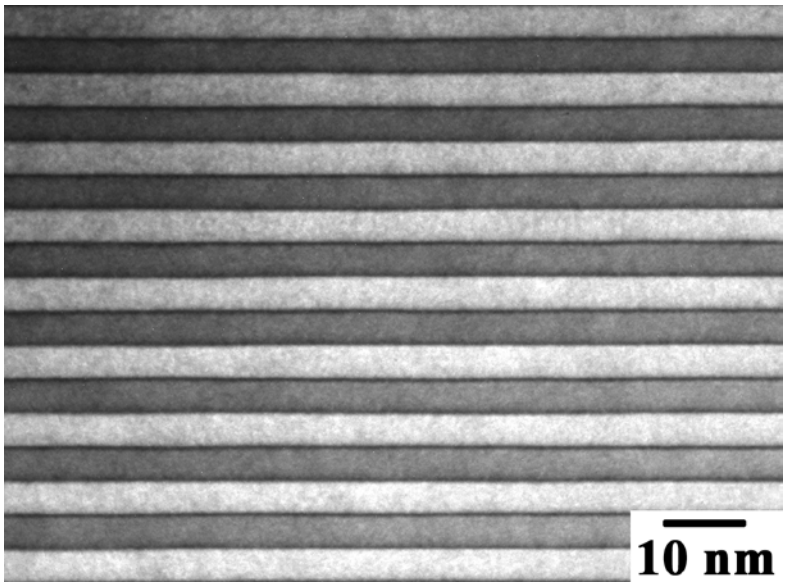

(a)

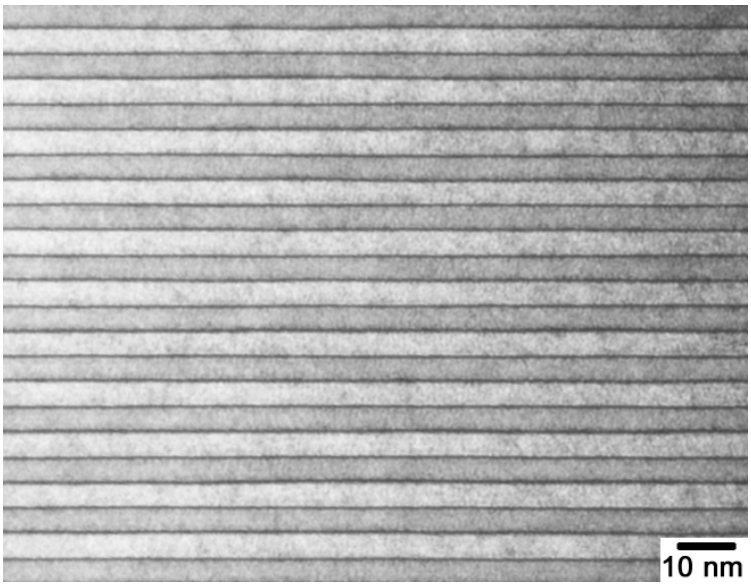

(b)

Figure 1. (200) dark-field images of InAs/GaSb superlattices showing (a) the structure with no interface control and (b) the structure with 0.8 ML InSb deposition at each interface.

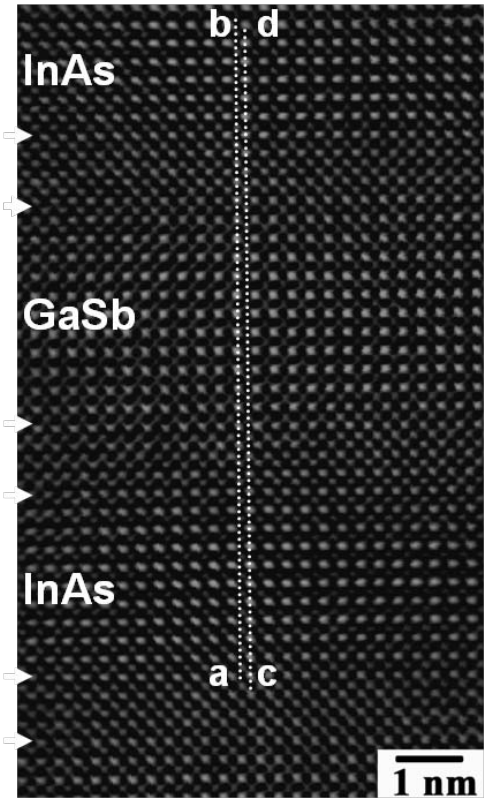

(a)

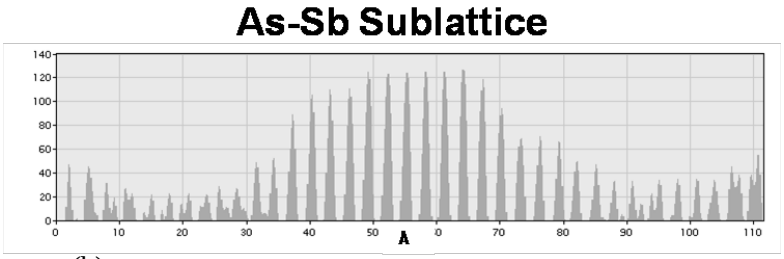

(b)

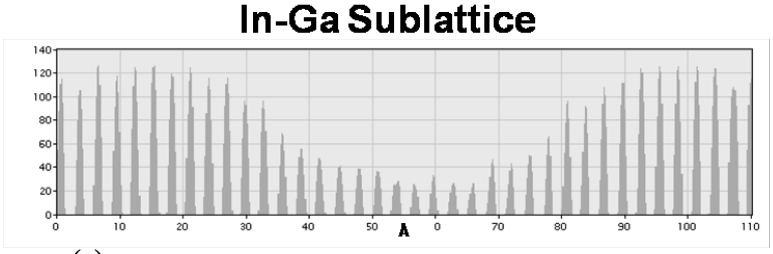

(c)

Figure 2. (a) Experimental phase image of the superlattice structure with no interface control. Arrows denote position of the interfacial regions. (b) Profile of the phase along the As-Sb sublattice denoted by line a-b. (c) Profile of the phase along the In-Ga sublattice denoted by line c-d.

To extract the composition profiles from the phase images a procedure based on factorial analysis of correspondence has been developed previously. A detailed description of this

procedure is provided in an earlier report. A flow chart describing this procedure is shown in Figure 4. The steps described in this flow chart is implemented in the following manner.

- Analysis is performed one column at a time, including only sublattices along line "a-b," (see Figures 2(a) and 3(a)).
- Cation and anion sublattices are analyzed independently.

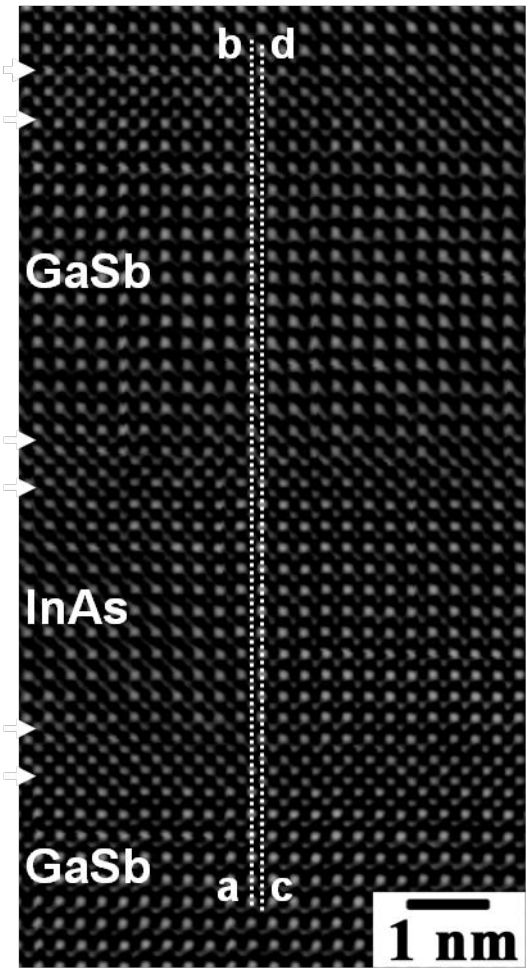

(a)

Figure 3. (a) Experimental phase image of the superlattice structure with interface control. Arrows denote position of the interfacial regions. (b) Profile of the phase along the As-Sb sublattice denoted by line a-b. (c) Profile of the phase along the In-Ga sublattice denoted by line c-d.

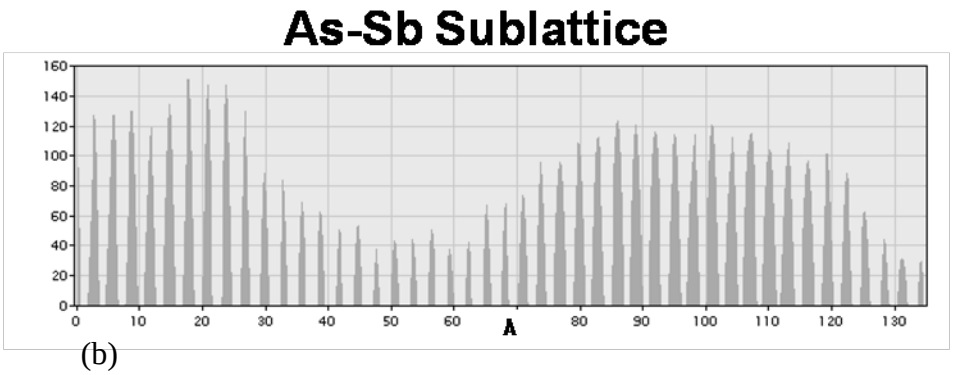

(b)

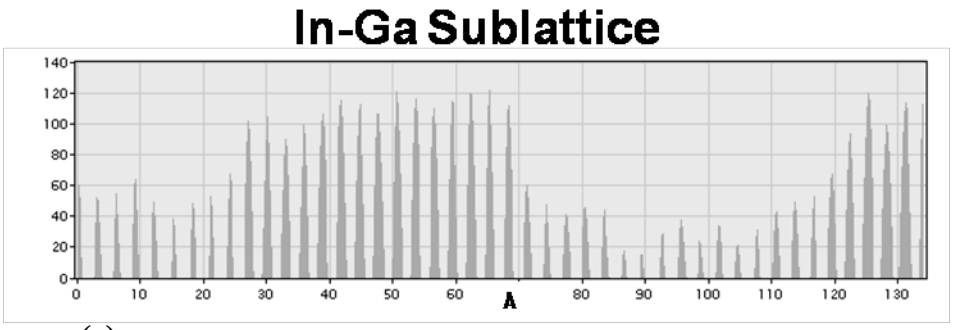

(c)

Figure 3. Continued.

- .The average values of the factorial coefficients C_1, (C_{avg}), of the InAs and GaSb layers away from the interfaces are determined.
- The x_{Ga} and x_{Sb} for each atomic column in the interface is calculated using C_{avg} determined from InAs and GaSb layers.

We note that the FAC procedure used for quantifying the phase images is developed based on an analysis performed on simulated images of bulk alloys. In this report the validity of its extension to heterointerfaces is examined, based on image simulations performed on model InAs/GaSb/InAs structures with abrupt and graded interfaces. Although the lattice constants for GaSb (a_{GaSb} = 0.610 nm) and InAs (a_{InAs} = 0.606 nm) are similar, the mismatch in the vicinity of interfaces is significant for both InSb-like (a_{InSb} = 0.647 nm) and GaAs-like (a_{GaSb} = 0.565 nm) interfaces. To include interfacial strain effects in our calculation we invoke a simple model, in which the basic unit is a (001) cross-section bi-layered slab consisting of a GaSb layer sandwiched between two InAs layers. The atomic arrangement at the interface is such that the InAs-on-GaSb (normal) interface is Ga-As bonded and the GaSb-on-InAs (inverted) interface is In-Sb bonded. Theoretical studies indicate that in the bulk state, the lattice distortions in these interfaces are nearly tetragonal and are confined to regions within 2 ML close to the interface

(23). In the case of thinned cross-sectional TEM samples strain relaxation is possible, depending on the ratio of the sample thickness to the superlattice period (24), due to reduced confinement normal to the surface. In the present study a detailed modeling of the strain relaxation is not attempted, since the values of these displacements are not used in calculating the local composition. Rather, the objective is to investigate the impact of (distortion induced) changes in the local phase values within sub-cells in the interfacial regions on the composition profiles determined using the FAC analysis.

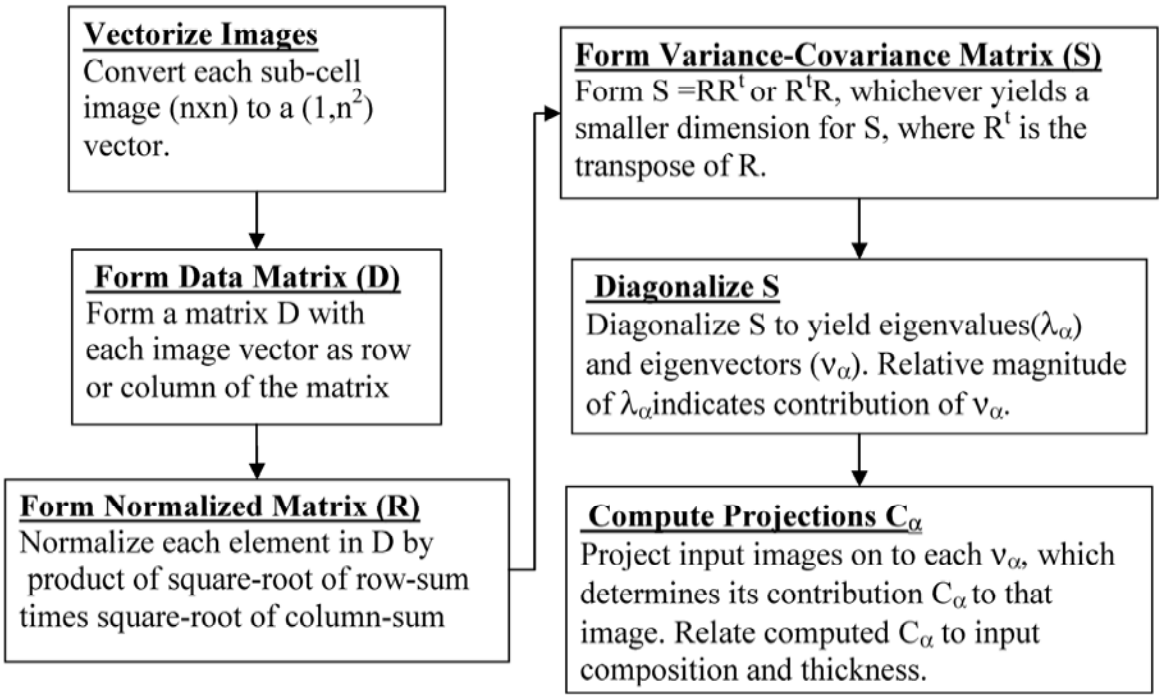

Figure 4. A flow-chart showing the sequential steps in the implementation of the FAC procedure.

The calculations are performed based on a model in which the distortions at each interface are assumed to be purely tetragonal, resulting in an expansion in the lattice normal to the interface at inverted ("InSb-like") interface and conversely, a contraction at the normal ("GaAs-like") interface. A sample of given thickness is then simulated by stacking the required number of slabs, with the spacing between each slab being 0.303nm. Simulations were performed with the model sample composed of four types of slabs, each having a GaSb layer of different thickness. Specifically, keeping the relative position of the inverted interface the same in all the slabs, the GaSb layer thickness was systematically increased in one monolayer (ML) steps from 7 ML(≈ 2.1 nm) thru 10 ML(≈ 3.0 nm) by an appropriate shift in the position of the normal interface. By stacking slabs of different types it is possible to generate structures with an

abrupt inverted interface and a graded normal interface, wherein the composition profile across the graded interface (averaged over all the slabs in the stack) is determined by the number of each type of slab included in the stack. Depending on the sequence in which the individual slabs are stacked, the strain induced atomic displacements in the graded interfacial region are described in terms of the changes in position of the normal interface within the stack. Since the stacking sequence can be changed arbitrarily, the model also permits investigating whether the arrangement of different atomic species within any given column has an influence on its computed composition.

The simulations were performed with slabs of size 64 ML (≈19.2 nm) x 8ML (≈2.4 nm), with the longer side being normal to the interfaces. Thru-focus series of HRTEM images of several model structures having different input composition profiles were simulated, for same settings of the microscope as those used in the experiment. The EPWF of each structure was then retrieved using the TrueImage software, and subsequent analysis of the resulting phase images was performed using the FAC procedure described earlier. Although the analysis was performed for both sublattices, only the results pertaining to the As-Sb sublattice is presented, noting that similar behavior was also observed for the In-Ga sublattice. Figure 5 shows typical results obtained from an analysis of the As-Sb sublattice of different structures with the same (averaged) input composition profile for the graded interface. It is evident that even in the presence of interfacial strain there is good agreement between the input composition profile and those determined from the reconstructed phase images. Among several such models examined, maximum deviation occurred for the structure with all Sb atoms in the graded interface located in the top-half of the atomic column. As shown in Figure 9, in this case the computed Sb composition profile was consistently lower than the input profile by about 0.06.

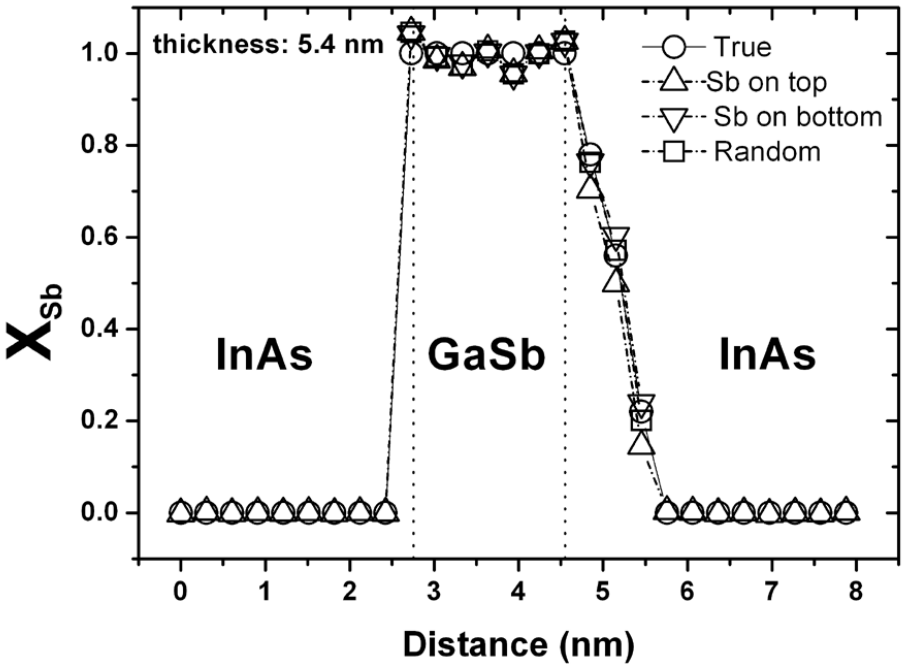

Figure 5. Plots from FAC analysis performed on the As-Sb sublattice in simulated phase images of InAs-GaSb-InAs model structures with abrupt (left) and graded(right) interfaces.

The results obtained upon applying the FAC procedure to phase images in Figures 2(a) and (a) are presented in Figures 6 and 7. The plots clearly show that untailored interfaces exhibit significant compositional grading in both the group-III and group-V sublattices. In the case of tailored interfaces, significant improvement in compositional abruptness is achieved at the GaSb-on-InAs interface, as shown in Figures 6 (a) and (b). A comparison of the plots shown in Figures 7 (a) and (b) reveal that this effect is however observed to be less dramatic at the InAs-on-GaSb interface. To correlate the measure composition profiles with measured properties, the photoresponse spectra from the two samples are shown in Figure 8. It is observed that the cutoff wavelength of sample with no interface control (7.7 μm) is significantly shorter than the pre-designed value of 10 μm. Theoretical calculations (25) have shown that the superlattice band gap energies increase (decrease) with reduction in the InAs (GaSb) layer thickness and that this behavior is especially more sensitive to changes in the InAs layer thickness. The reduced cutoff wavelength may explained by the reduced InAs layer thickness, indicated by composition profiles at the GaSb-on-InAs interface.

The reduction in the InAs layer thickness in the sample with no interface control could be due the well known Ga-into-In exchange reaction, which would be expected to be dominant at the GaSb-on-InAs interface. Our results suggest that pre-deposition of InSb at the GaSb-on-

InAs interface tends to preserve the intended thickness of the InAs layer by acting as a barrier layer limiting the In-Ga exchange mechanism.

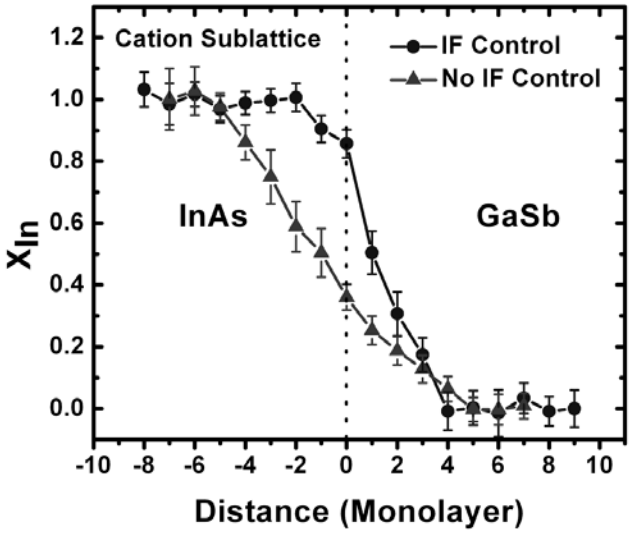

(a)

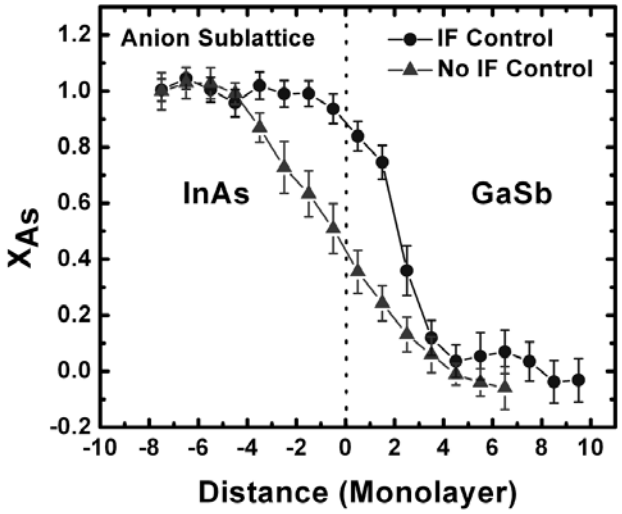

(b)

Figure 6. Plots showing the averaged composition profiles across the GaSb-on-InAs interface, along (a) the cation sublattice and (b) the anion sublattice.

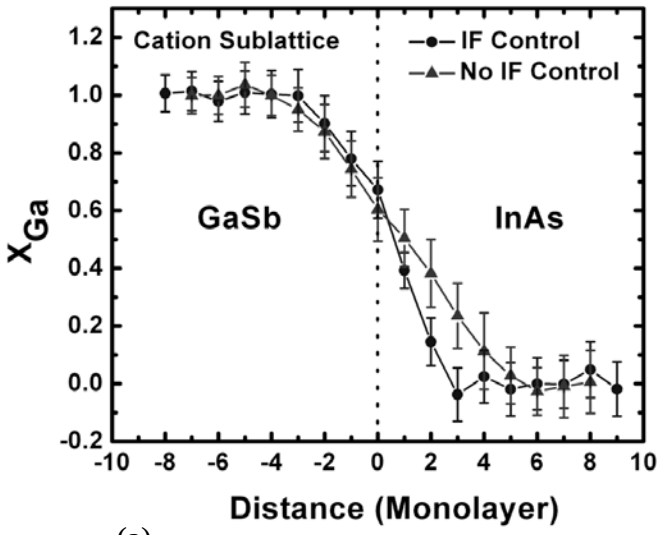

(a)

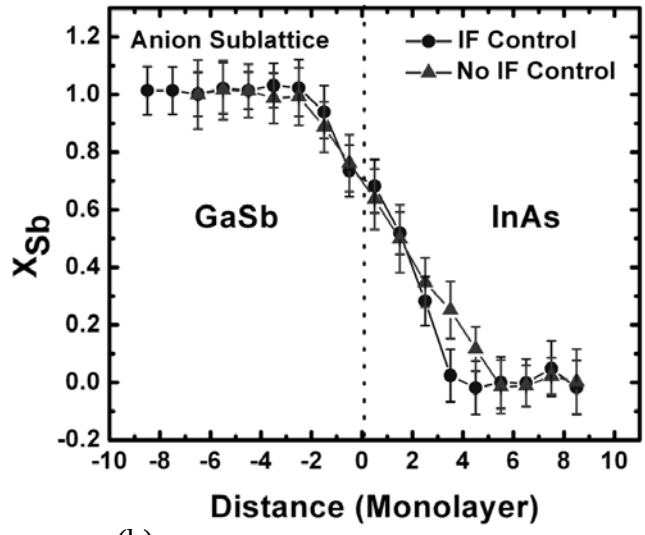

(b)

Figure 7. Plots showing the averaged composition profiles across the InAs-on-GaSb interface, along (a) the cation sublattice and (b) the anion sublattice.

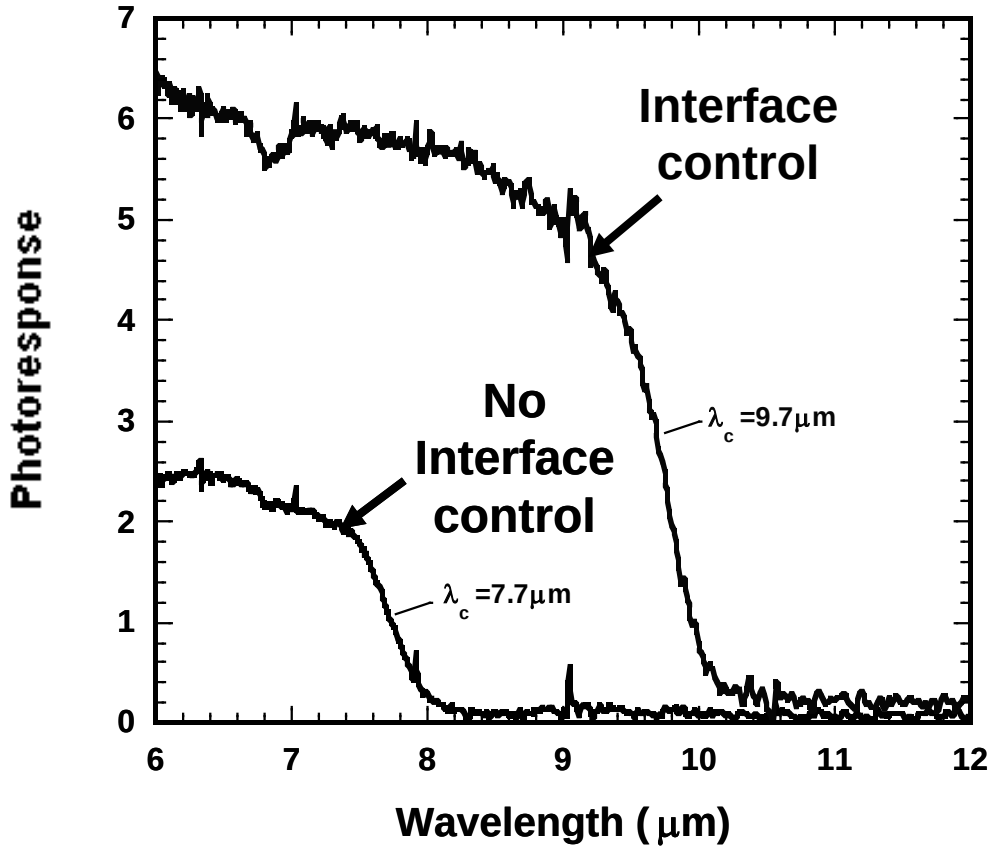

Figure 8. Plots showing the photoresponse spectra for superlattices with and without interface control.

3.2 TEM Characterization of InGaAs QDIP structures

The QDIP structures examined in this study consisted of InAs QDs grown on (100) GaAs substrates wherein each QD layer had a 20 ML-thick capping layer of $In_{0.15}Ga_{0.85}As$ which was followed by a 180 ML-thic GaAs spacer layer. Several samples with the number of QDIP stacks ranging from 1-20 were examined in this study. The diffraction patterns shown in Figure 9 represent the typical conditions used for imaging the QD layers. Specifically, the two-beam diffraction condition for obtaining the bright-field (G=200) and (200) dark-field images is shown in Figure 9 (a) and that for the bright-field (G=022) and (022) dark-field images in Figure 9 (b).

To facilitate a systematic study of the structural evolution with increasing number of QD stacks, an investigation was first performed on a sample containing a single QD layer. Figure 10 (a) is a bright-field (G=(022)) of the QD layer, in which the contrast due to the strain-field associated with the QDs is clearly visible. However, it is evident that no dislocation nucleation occurs in these regions. An examination of the (200) dark-field image, shown in Figure 10 (b), further reveals that the InGaAs layer is of uniform thickness. Figures 11-13 show the bright-

field (G=(022)) and (200) dark-field images of samples in which the number of 5, 10 and 20 QD stacks. From a comparison of these images with those shown in Figure 10, it is clear that there is no significant change in structural evolution with increase in number of QD layers. In particular, it is observed that structural integrity of each QD layer is well maintained with no evidence for nucleation/propagation of dislocations. The dislocation density in many of the above amples was evaluated by plan-view TEM. Figure 14 is a (220) dark-field image of the sample with a single QD layer showing a structure in which the QDs exhibit the typical Ashby-Brown contrast, indicating a high degree of coherency. Figure 15 is a (220) dark-field plan-view TEM image of the sample with 10 QD stacks. In this image the QDs are not visible due to presence of a thicker (3 μm) GaAs contact layer. In contrast to the single QD layer sample (Figure 14), the presence of dislocations is clearly observed in this sample. The oscillating contrast exhibited in these images indicates that the dislocations propagate from the bottom to the top surface of the film. Based on an analysis of several images similar to that shown in Figure 15, the dislocation density in this sample is estimated to be about 10^8 /cm^2. Noting that the image in Figure 15 and cross-sectional TEM images shown in Figure 12 are from the same sample, it is not possible to identify the source of these dislocations.

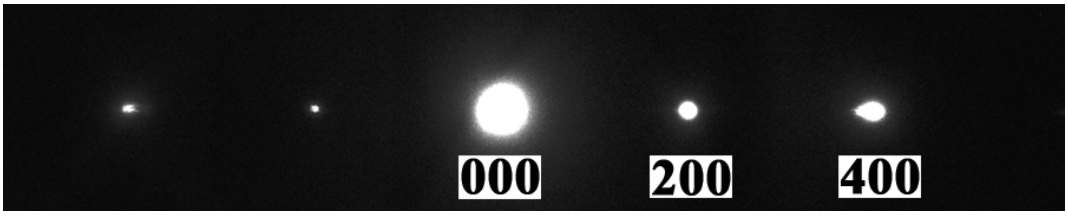

(a)

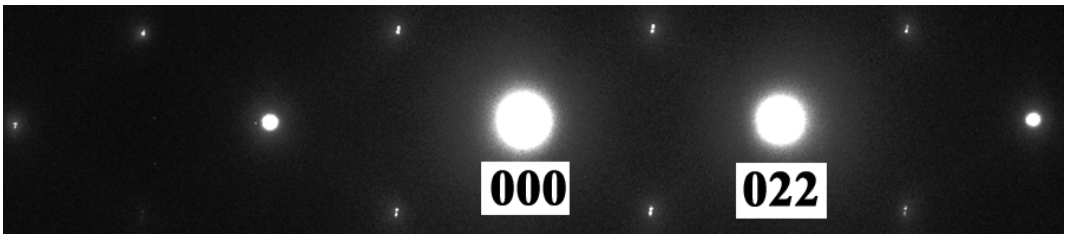

(b)

Figure 9. Diffraction patterns representing the two beam imaging conditions used for (a) G=200 and (b) G=022 bright-field and dark-field images.

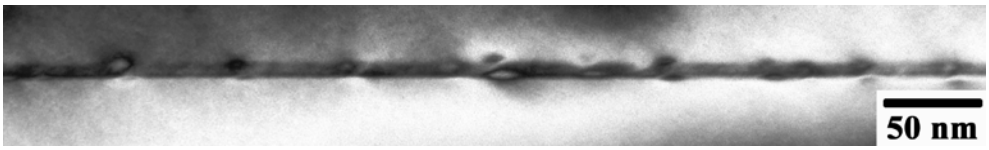

(a)

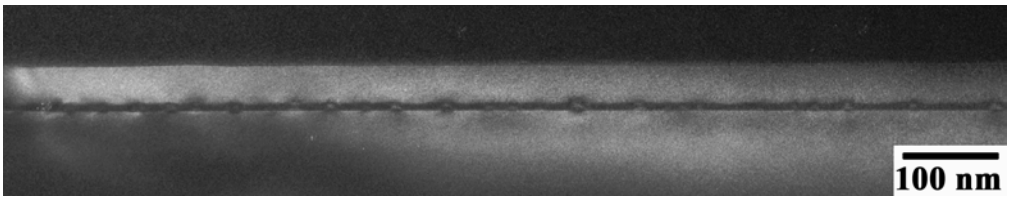

(b)

Figure 10. Cross-sectional TEM images of the single-layer QDIP structure showing (a) G=(022) bright-field image and (b) (200) dark-field image.

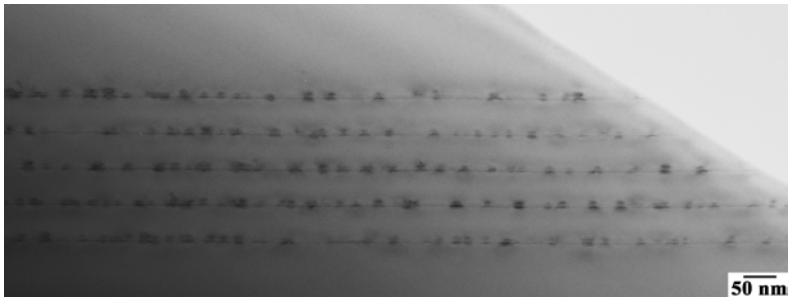

(a)

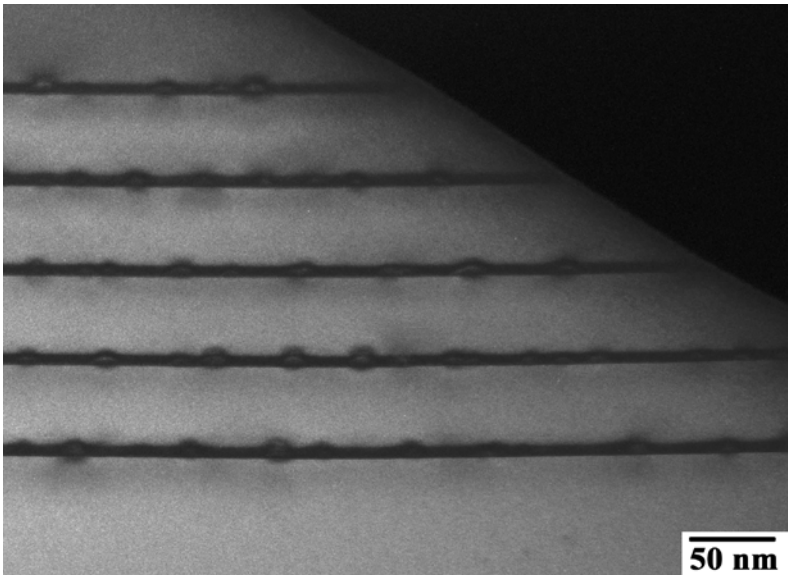

(b)

Figure 11. Cross-sectional TEM images of the 5-layer QDIP structure showing (a) G=(022) bright-field image and (b) (200) dark-field image.

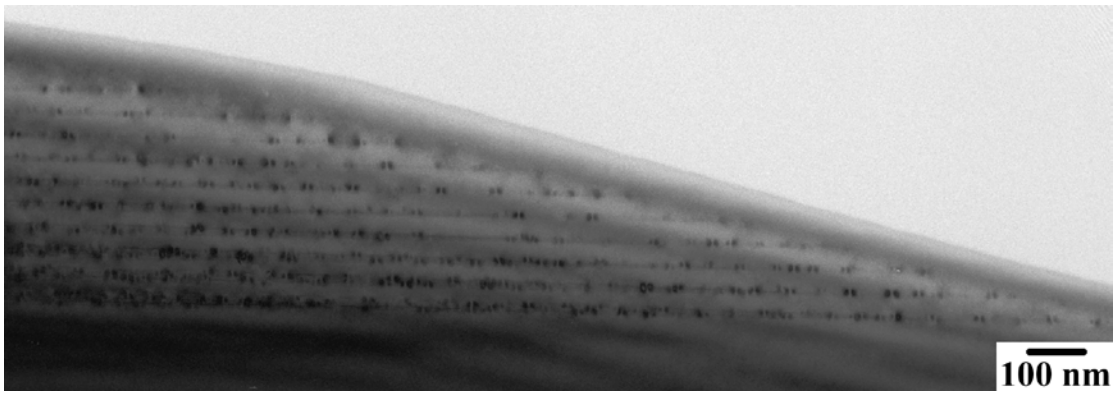

(a)

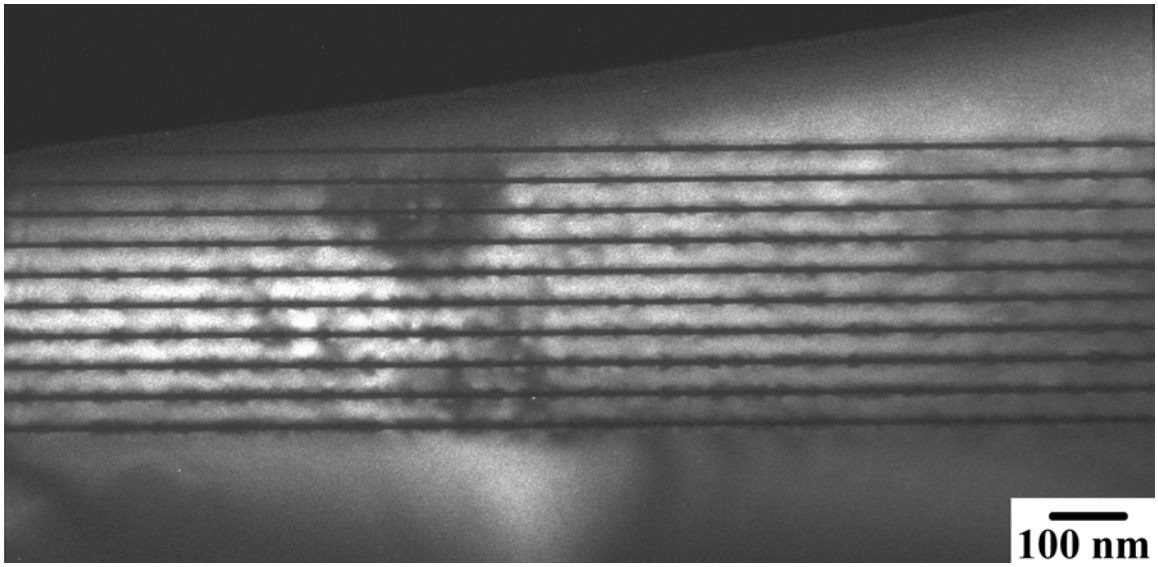

(b)

Figure 12. Cross-sectional TEM images of the 10-layer QDIP structure showing (a) G=(022) bright-field image and (b) (200) dark-field image.

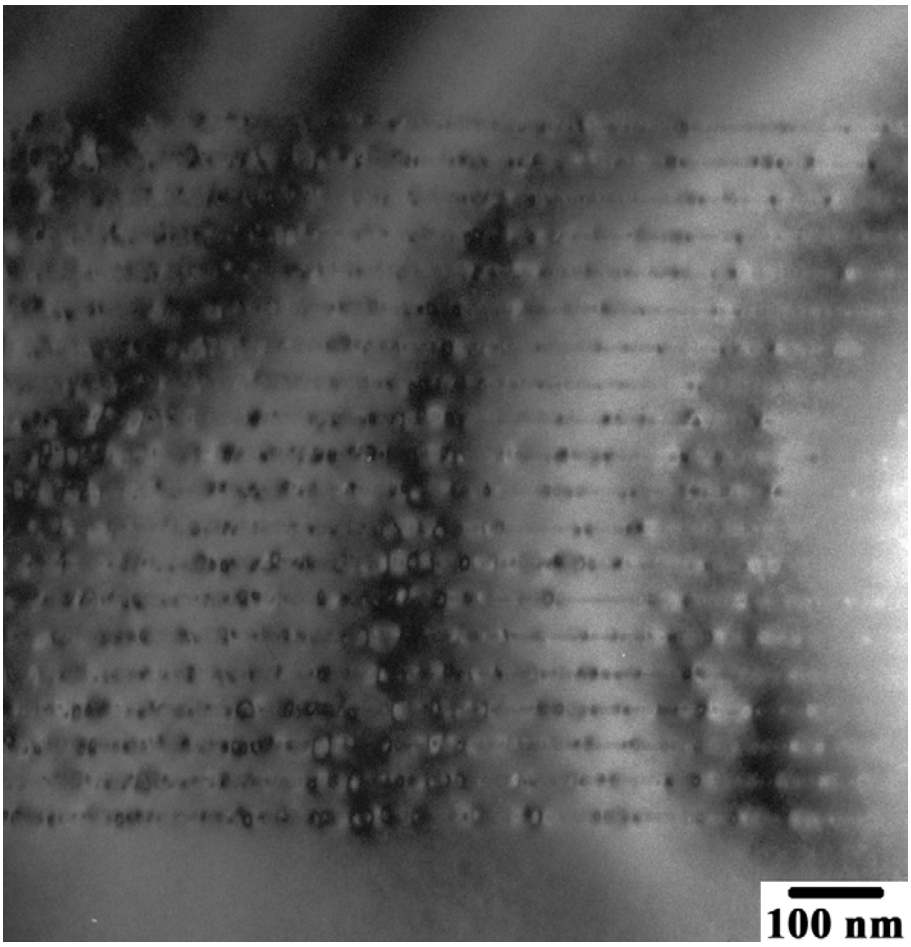

(a)

Figure 13. Cross-sectional TEM images of the 20-layer QDIP structure showing (a) G=(022) bright-field image and (b) (200) dark-field image.

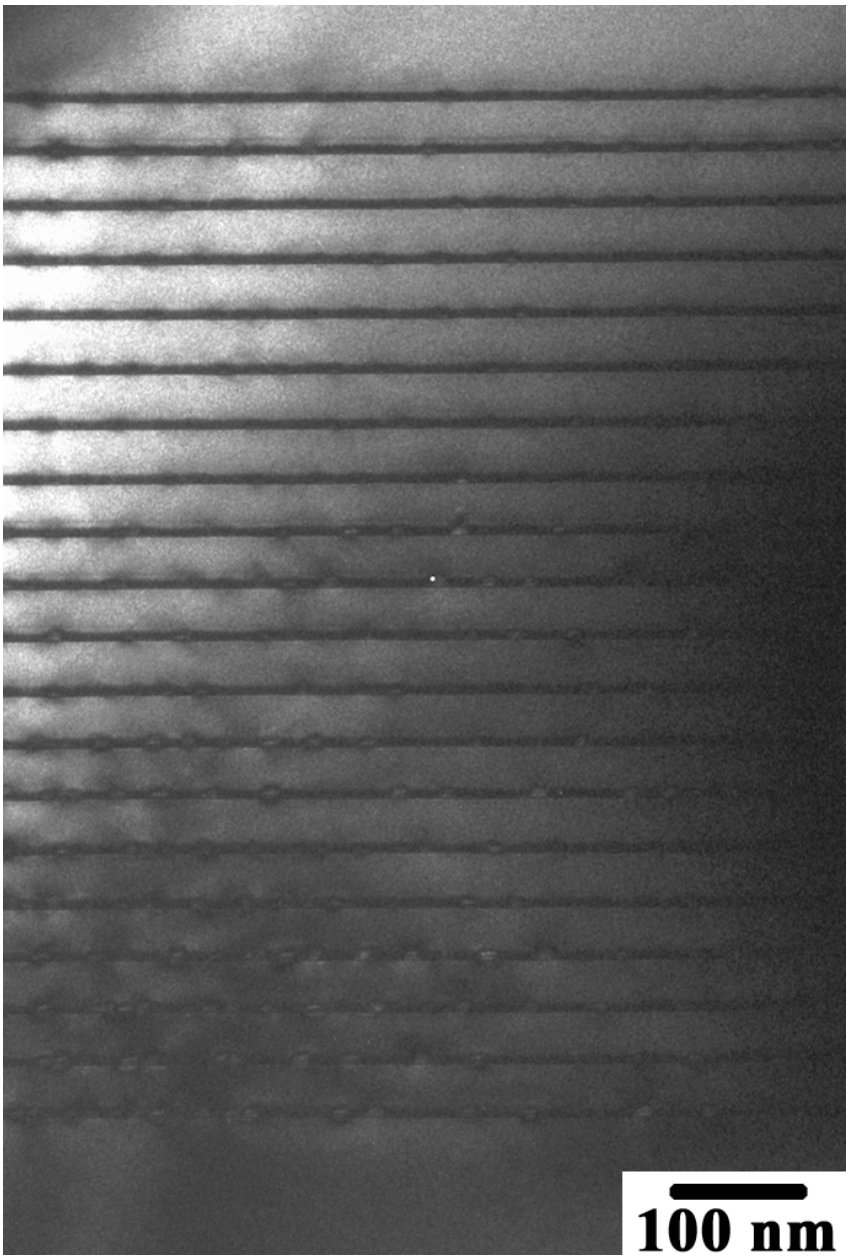

(b)

Figure 13. Continued.

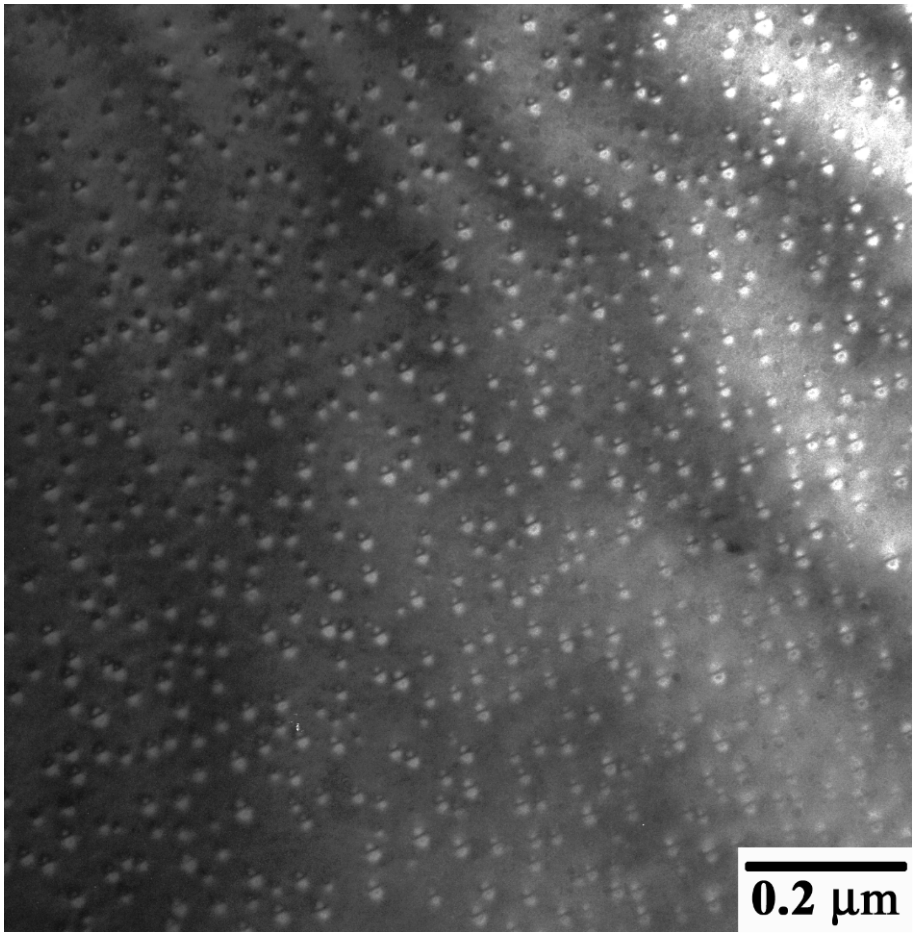

Figure 14. Plan-view TEM bright-field (G=(220)) image of the single-layer QDIP structure.

Figure 16 is a (220) dark-field plan-view TEM image of the sample containing 20 QD layers. In this case the QDs are clearly visible because the top GaAs contact layer was etched away prior to TEM observations. A comparison with the image of the single layer QD layer (Figure 14) shows that the two structure are similar, although a higher density of QDs are observed in the 20-layer structure in the thicker regions (right hand side in Figure 16) due to the overlap in layers when image in plan-view. The absence of dislocations observed in this sample indicates that the source of high dislocation density observed in the 10-QD layer sample could be the top GaAs contact layer. To verify this possibility the plan-view TEM observations on the 10-QD layer sample was repeated after the top GaAs contact layer was etched off. The (220) dark-field image, shown in Figure 17, reveals that the dislocations observed in Figure 15 are removed indicating that they originated during growth of the GaAs contact layer. Also, the QDs in this image are similar to those observed in the other plan-view TEM images (Figures 14 and 16), thereby indicating that the defect density in the QD stack is low, as in the single layer and 20-layer QDIP samples.

3.3 M-Structure: AlSb-Containing Superlattices

The sample examined is a 100-period superlattice structure consisting of alternating layers of InAs: 4.8-4.9nm/ GaSb: 1.2nm/AlSb: 0.6-0.7nm/GaSb 1.2 nm, grown on a (100)-GaSb substrate. Figure 18 is a bright-field TEM image (G=(200)) showing the overall structure. The absence of layer undulations and dislocations in several such regions examined is indicative of a highly uniform structure with low defect density. A more detailed examination of the individual layers in the top and bottom regions of the superlattice (shown in Figure 19) showed that the average thickness of the InAs layer was 4.87 ± 0.12 nm and that for the GaSb layer 3.02 ± 0.14 nm.The layer thickness of GaSb also includes the AlSb layer in the middle, which is revealed as thin bright lines (indicated by arrows) in Figure 19(b). A deviation from the intended GaSb layer thickness was however observed in the bottom region of the sample (shown in Figure 19(a)), wherein the thickness of the 10^{th} and 14^{th} layers were about 10 nm.

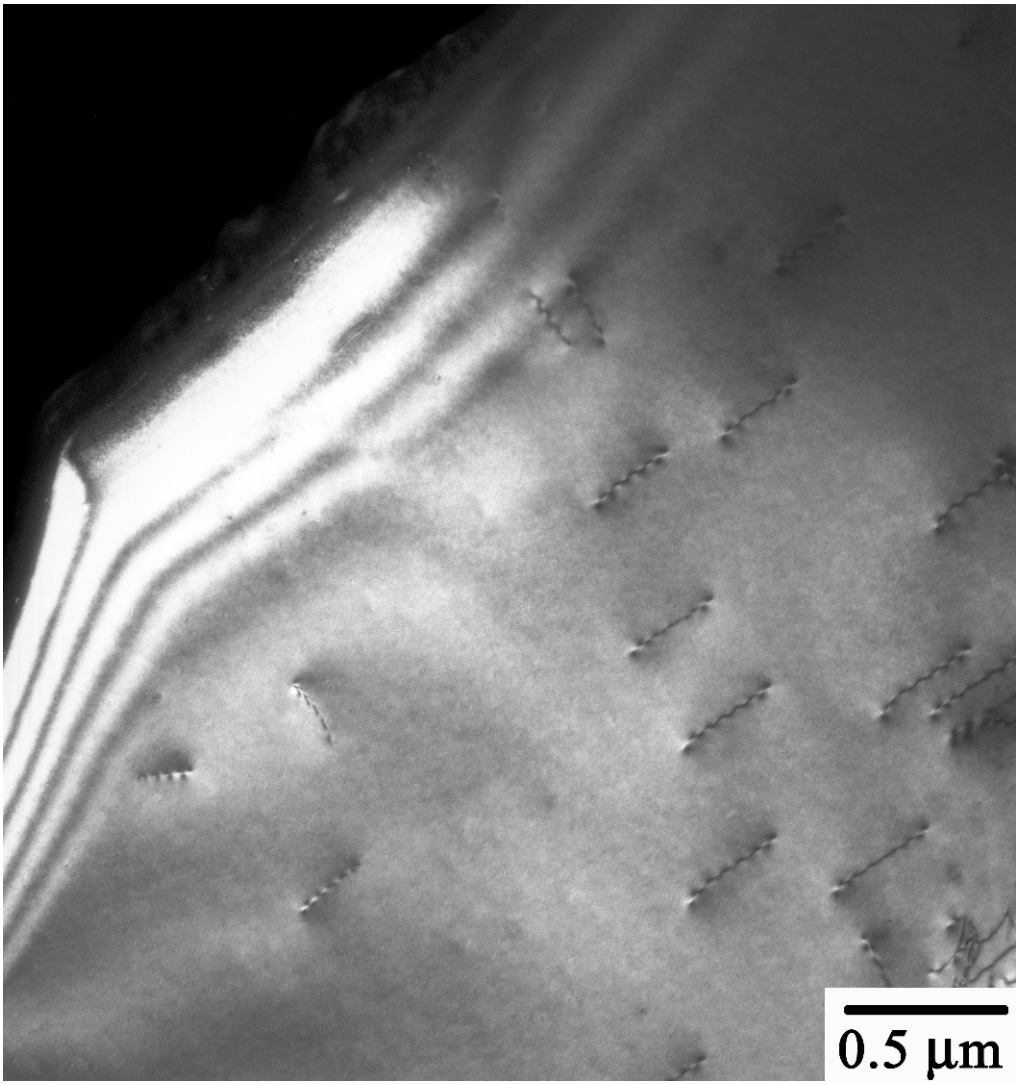

Figure 15. Plan-view TEM bright-field (G=(220)) image of the 10-layer QDIP structure with the top GaAs-contact layer.

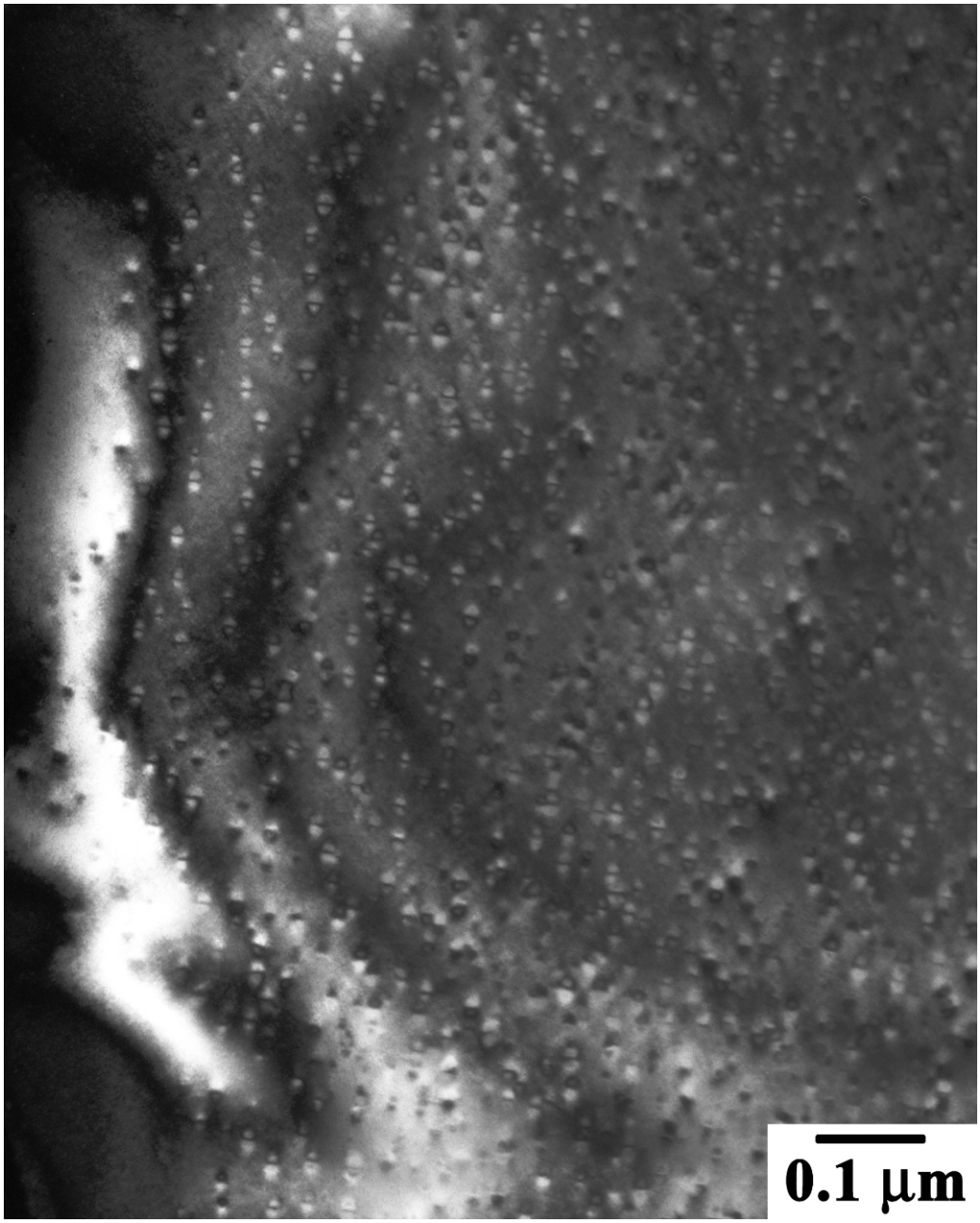

Figure 16. Plan-view TEM bright-field (G=(220)) image of the 20-layer QDIP structure with the top GaAs-contact layer removed.

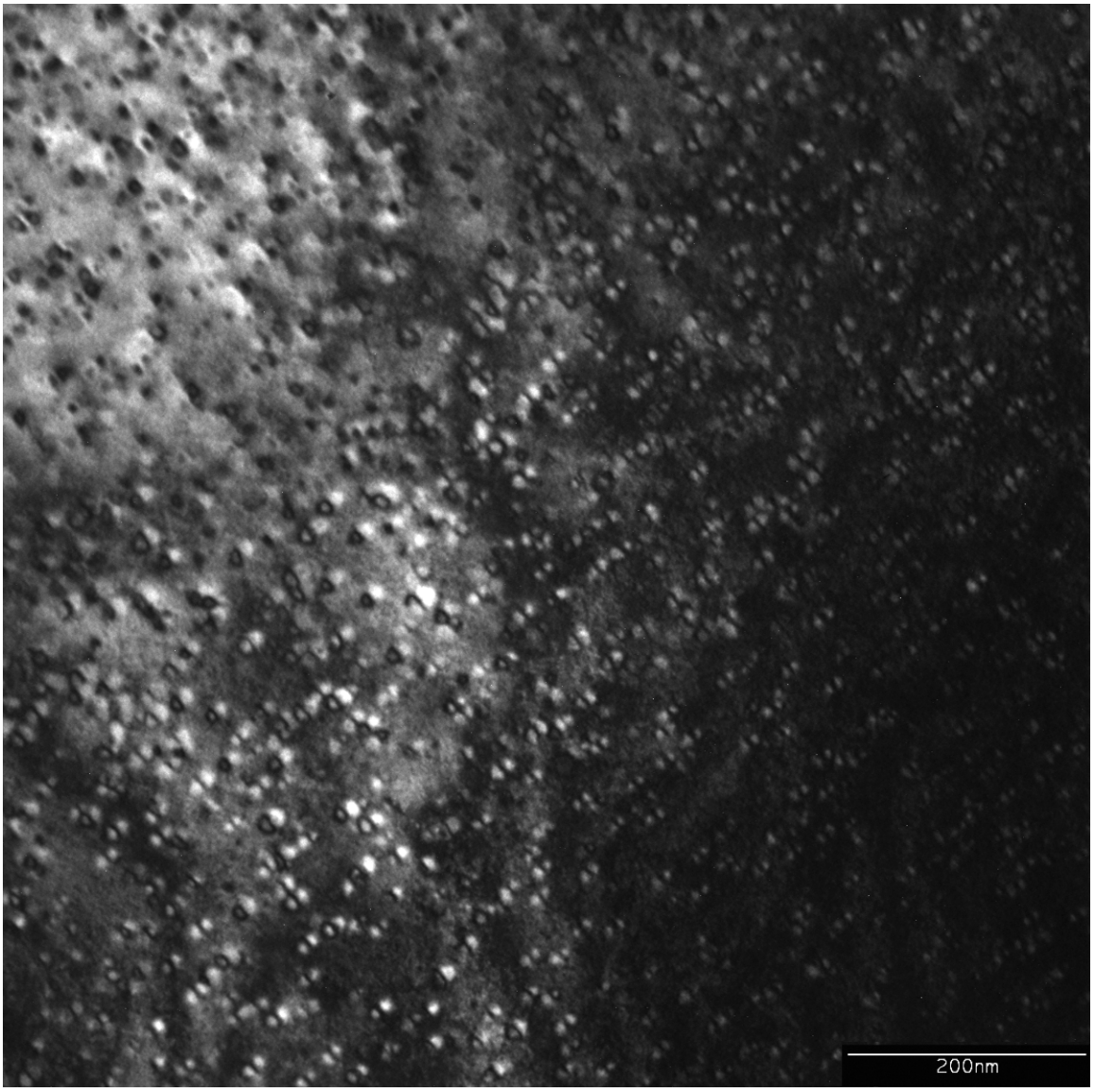

Figure17. Plan-view TEM bright-field (G=(220)) image of the 10-layer QDIP structure with the top GaAs-contact layer removed.

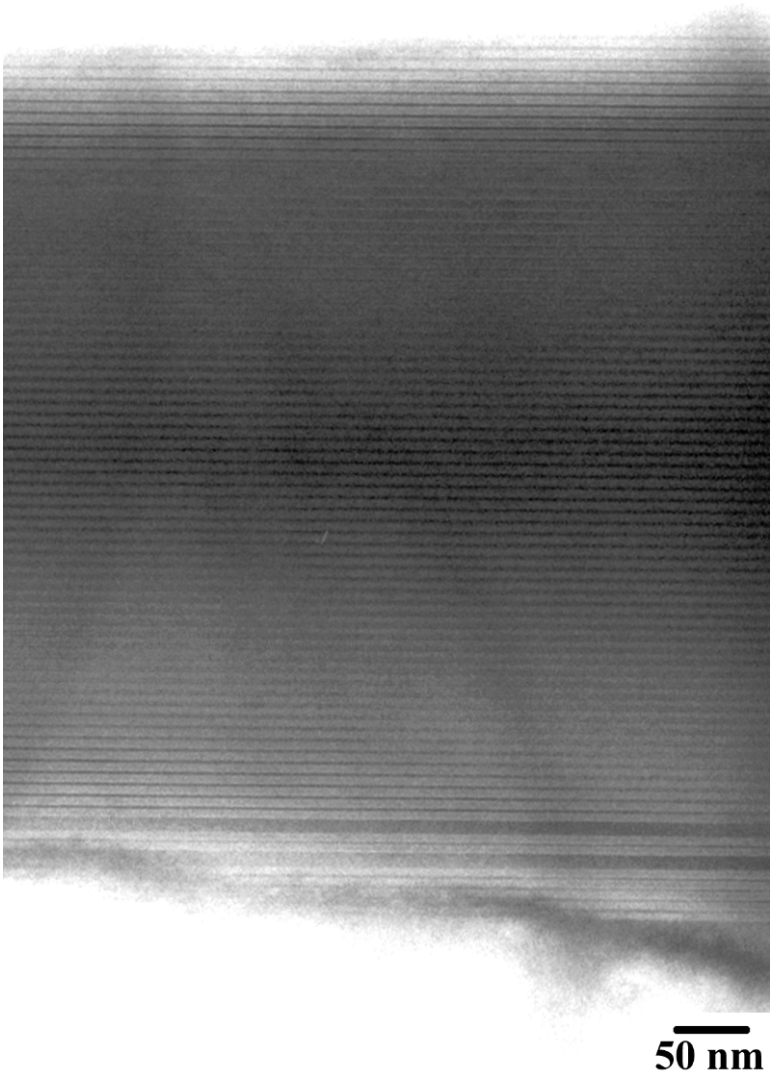

Figure 18. Bright-field (G=200) image of the M-structure.

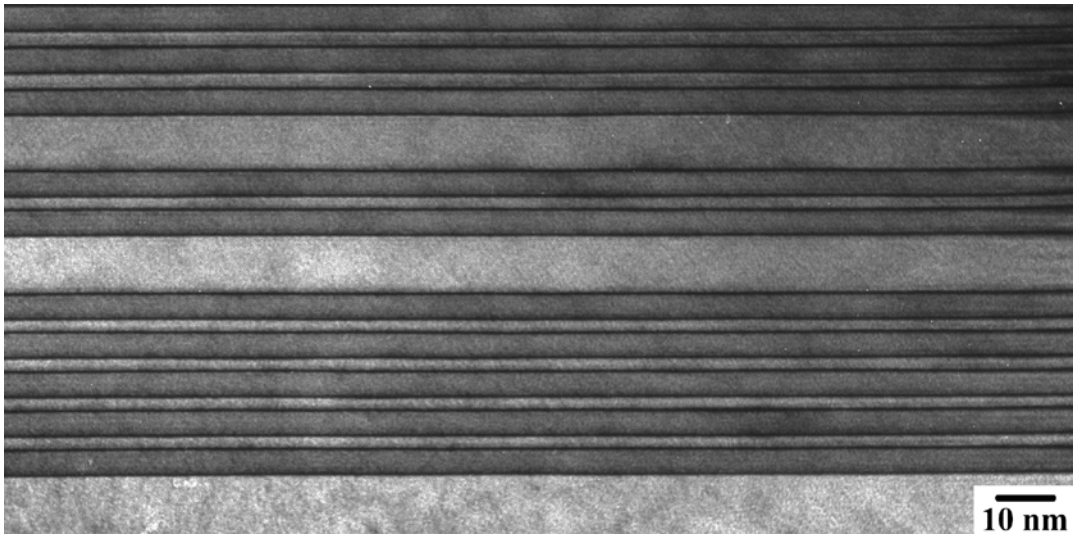

(a)

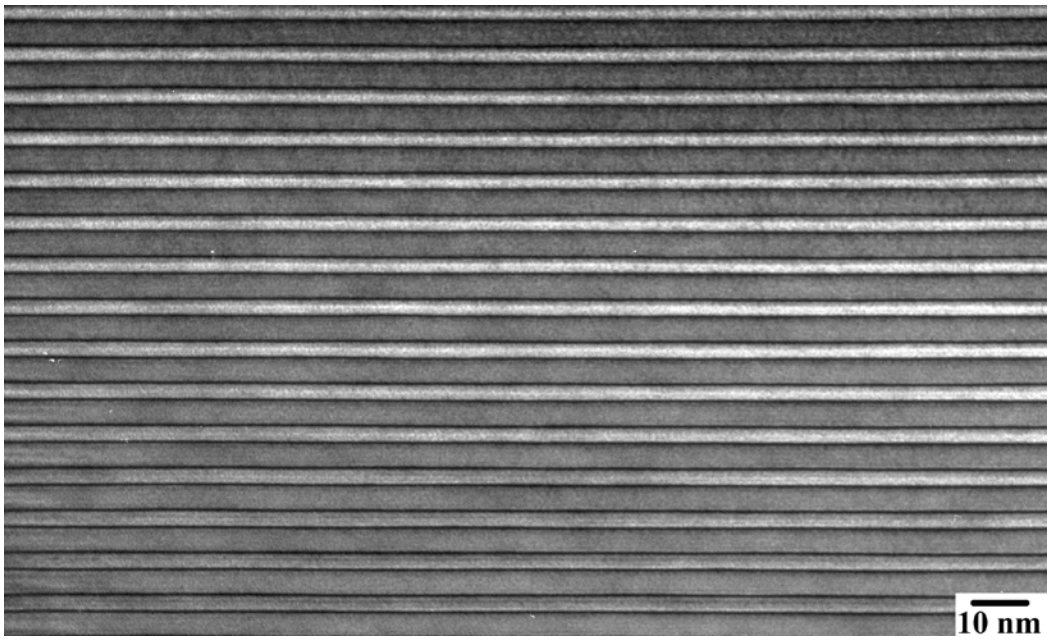

(b)

Figure 19. (200) dark-field TEM image of the M-structure showing the InAs (thick) and the GaSb (thin) layers in the (a) bottom and (b) top regions of the sample.

3.4 9.5 μm QCL Device Structure

The sample examined is a quantum cascade laser structure containing alternating AlInAs/GaInAs barrier/well layers grown on a (100) InP substrate. The device design consisted of 50 active/injector stages (total nominal thickness of 3μm), with each active and injector region containing 7 and 4 well/barrier pairs, respectively. Figure 20(a) is a bright-field (G=200) image of the overall structure revealing the presence of a dislocation in the InP cladding layer. An examination of the active/injector layers on the substrate- side (Figure 20 (b)) showed the presence of undulations in the first layer grown on the substrate. A more uniform structure is however observed in the subsequent layers. Shown in Figure 21 is a TEM image of the active/injector region in the middle part of the structure, wherein the AlInAs-barrier and InGaAs-well layers appear dark and gray, respectively. From these images the thickness (nm) of the well/barrier pairs in the injector regions were measured to be 3.4/1.4, 3.6/1.4, 3.0/1.6, 3.4/1.8, 2.8/2, 2.6/2.8 and 3.8/4.2. Within the active regions, the thickness (nm) of the well/barrier pairs were measured to be 0.8/1.8, 5.2/1.6, 4.8/1.4 and 4.6/2.6. It should be noted that the accuracy of these measurements (±0.4 nm) was somewhat compromised due to inter-diffused nature of the interfaces (especially in the case of thicker AlInAs layers) and also due to the sample preparation artifacts arising from amorphous layers on the top and bottom surfaces of the sample.

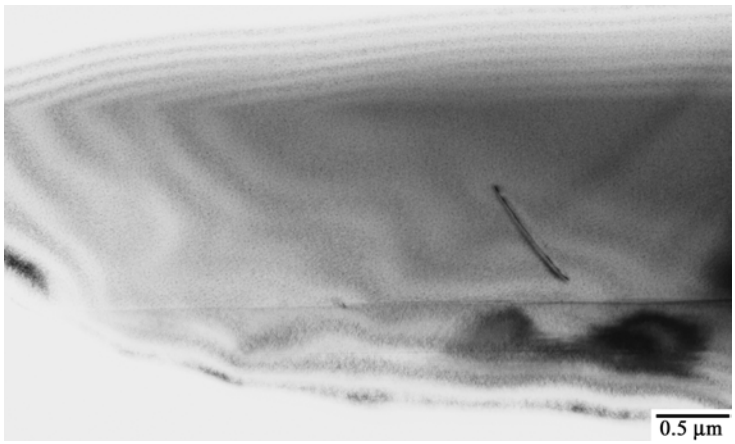

(a)

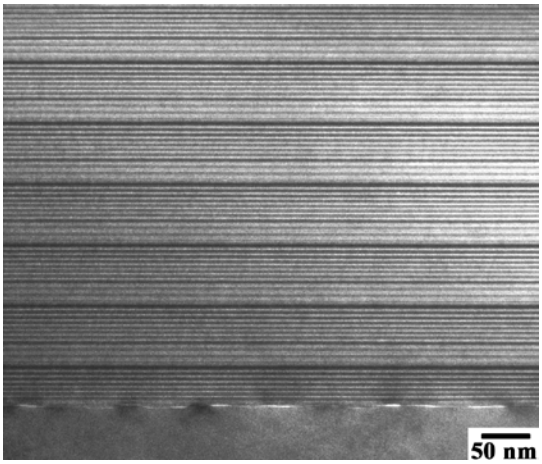

(b)

Figure 20. Bright-field image (G=(200) of the QCL device structure showing (a) the presence of a dislocation in the top InP cladding layer, and (b) the active/injector regions near the substrate where undulations in the first layer on top of the substrate are visible.

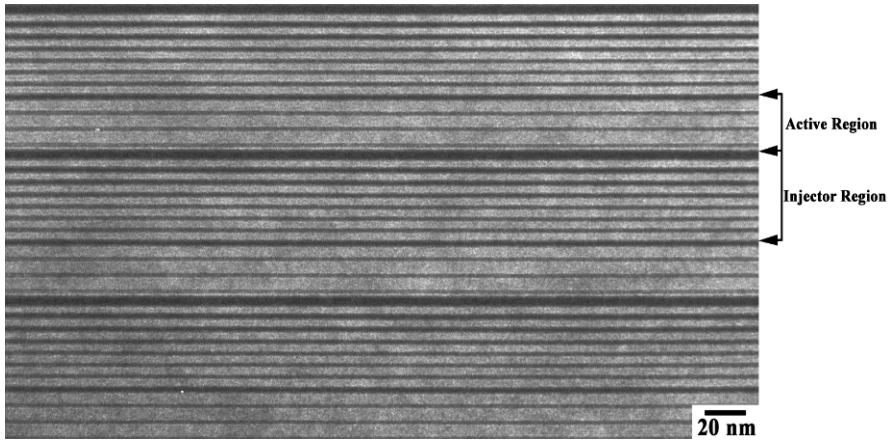

Figure 21. TEM image of the active/injector regions in the QCL device structure showing the individual AlInAs-barrier (dark) and the GaInAs-well (grey) layers.

3.5 InGaAs-InAlAs QWIP Structures

The structure examined is a QWIP structure consisting of a 25 period $In_{0.53}Ga_{0.47}As$/ $In_{0.52}Al_{0.48}As$ well/barrier layers grown on a (100) InP substrate. The nominal thickness of barrier and well layers were 28.6 nm and 3.5 nm, respectively. As observed in the bright-field image shown in Figure 22 (a) the overall structure exhibits very high quality. The uniformity of the constituent layers is also evident in the (200) dark-field images shown in Figure 22(b). The average thickness of the $In_{0.53}Ga_{0.47}As$ and $In_{0.52}Al_{0.48}As$ layers were measured to be 3.73 (±0.33) nm and 35.36 (±0.35) nm.

3.6 QDIP Structures with InGaP Barrier Layers

The samples examined are 10-period quantum-dot infrared photo-detector structures grown on (100) semi-insulating GaAs substrates, consisting of $In_{0.68}$ $Ga_{0.32}As$ quantum-dots enclosed within InGaP barriers, with each period being separated by a 100 nm-thick InGaP spacer layer. Three samples with different barrier layers were examined: (1) sample-N3313 in which the InGaP barrier layer thickness was 35 nm, (2) sample- N3398 in which the InGaP barrier layer was 35 nm in thickness, but with the initial 6nm grown at a lower temperature and (3) sample N3236 in which the barrier layer consisted of an initial 2.7 nm thick GaAs and a subsequent 32.3 nm thick InGaP layer.

Figure 23 (a) is a bright-field (G=200) of the structure in sample –N3313 showing a highly irregular structure, triggered by defect formation occurs during the initial stages of growth. A closer examination of the first QDIP layer, shown in Figure 23(b), reveals that

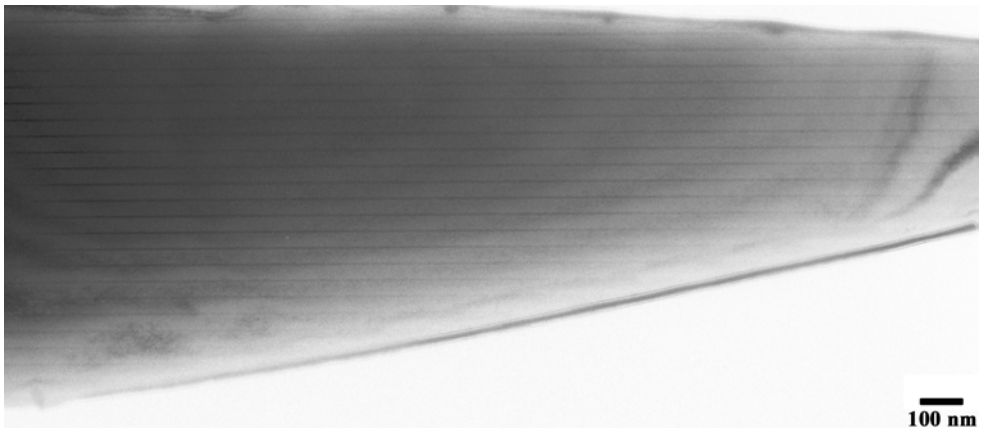

(a)

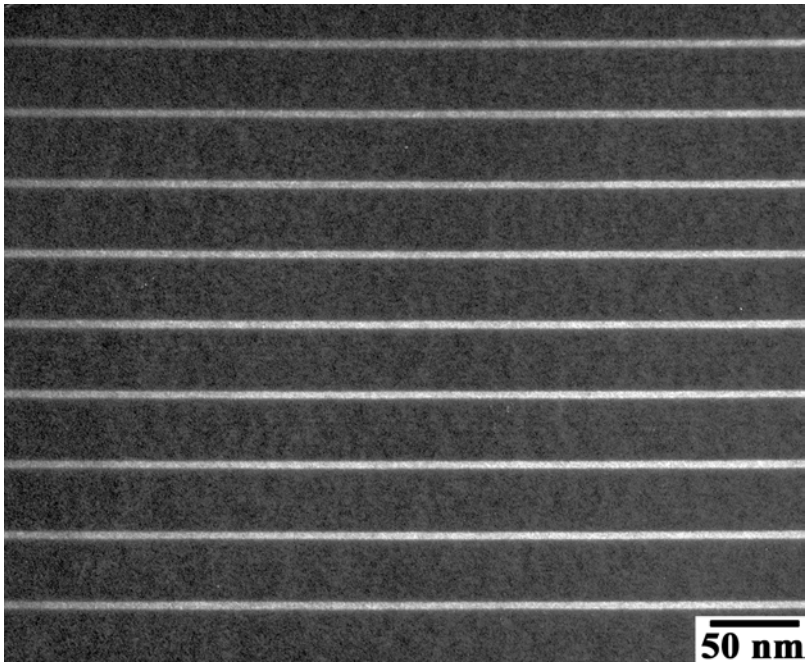

(b)

Figure 22. (a) Bright-field and (b) dark-field (G=200) TEM images of the QWIP structure showing the $In_{0.53}Ga_{0.47}As$ well (thin) and the $In_{0.52}Al_{0.48}As$ (thick) barrier layers.

3.7 QDIP Structures on InP Substrates

The samples examined are 10-period QDIP structure grown on an InP substrate, consisting of InAs QDs with each period separated by a 40 nm InP spacer layer. Two samples were examined: (1) Sample-EMC 2050 in which the deposition of InAs QDs was preceded by the growth of a 3 nm thick $In_{0.52}Al_{0.48}As$ and a 1 nm thick GaAs layer and (2) Sample-EMC 2399, in which the deposition of InAs QDs was preceded by the growth of a 1 nm thick GaAs layer and followed by a deposition of 1 nm thick $In_{0.53}Ga_{0.47}As$ layer. Figure 27 (a) and (b) are

(200) dark-field images of the two samples investigated. Both structures exhibit similar features, characterized by an onset of morphological instabilities in the InP spacer layers beyond the 3rd period in the QDIP structures. Evidence of defect formation is also observed in the sample-EMC 2050 (Figure 27 (a)).

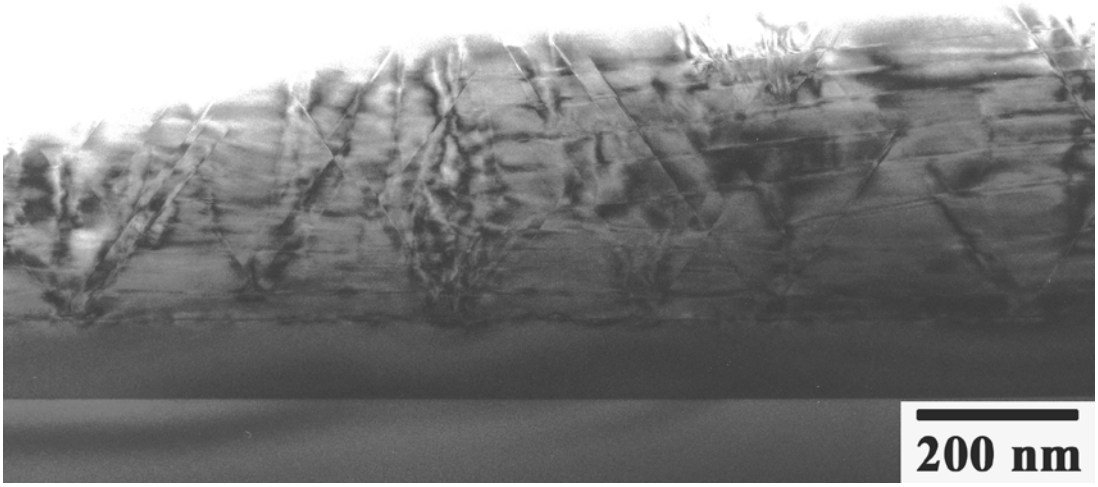

(a)

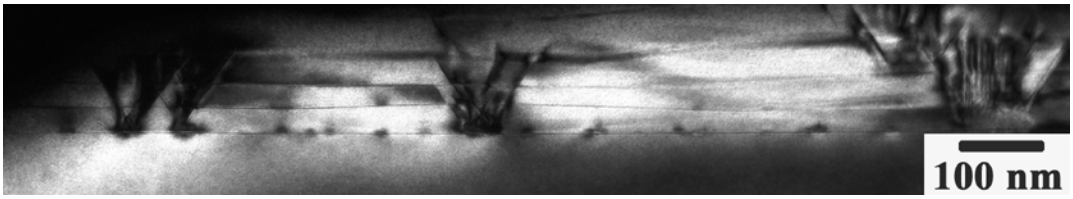

(b)

Figure 23. Cross-sectional TEM image of sample N3313 under (a) bright-field (G=200) and (b) (200) dark-field imaging conditions.

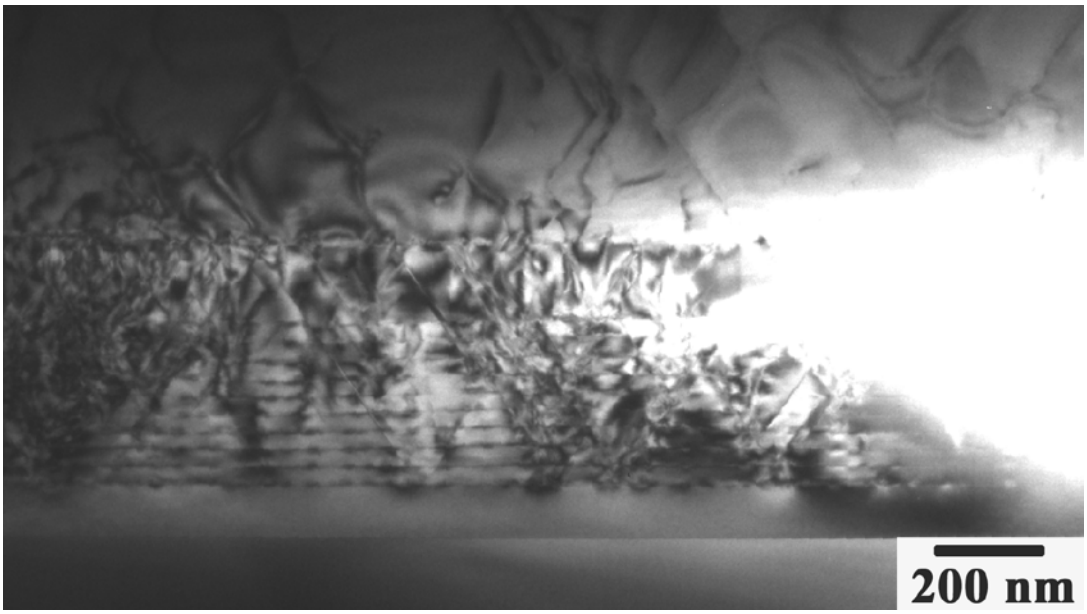

(a)

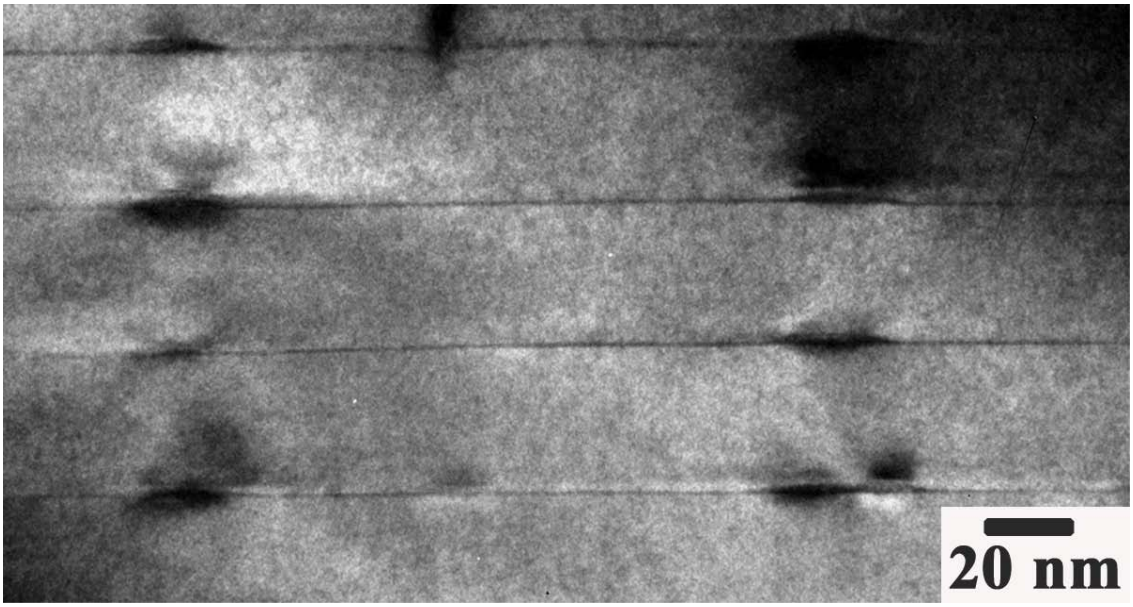

(b)

Figure 24. Cross-sectional TEM image of sample N3398 under (a) bright-field (G=200) and (b) (200) dark-field imaging conditions.

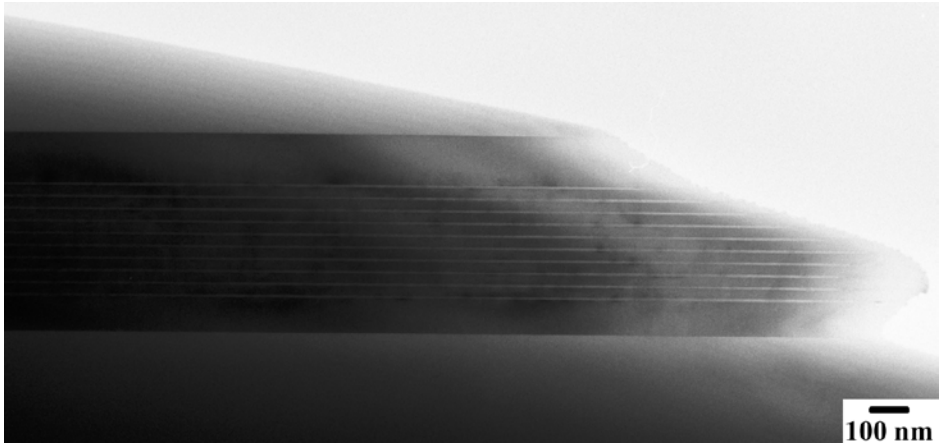

(a)

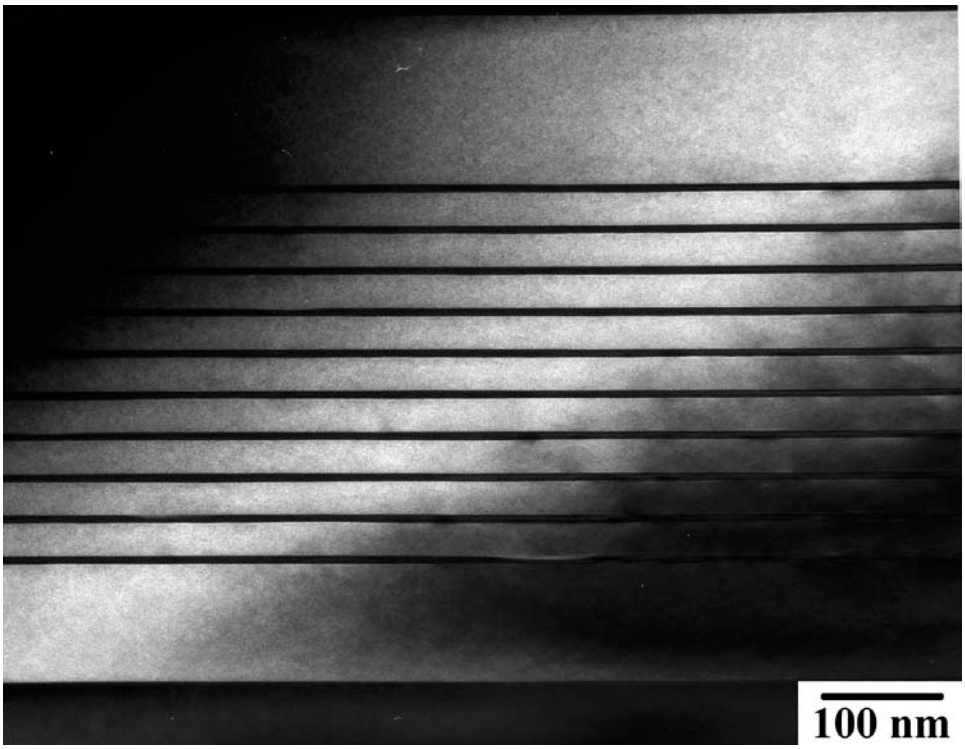

(b)

Figure 25. Cross-sectional TEM image of sample N3236 under (a) bright-field (G=200) and (b) (200) dark-field imaging conditions.

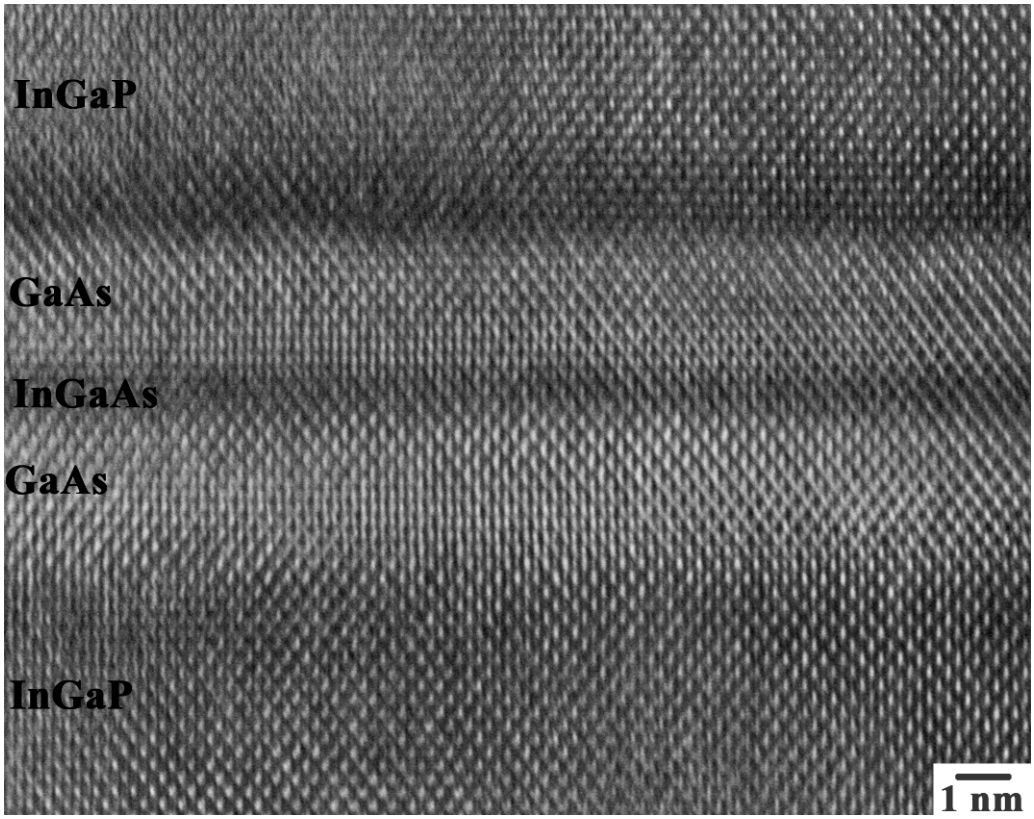

Figure 26. High-Resolution TEM image of a buried InGaAs layer in sample 3236.

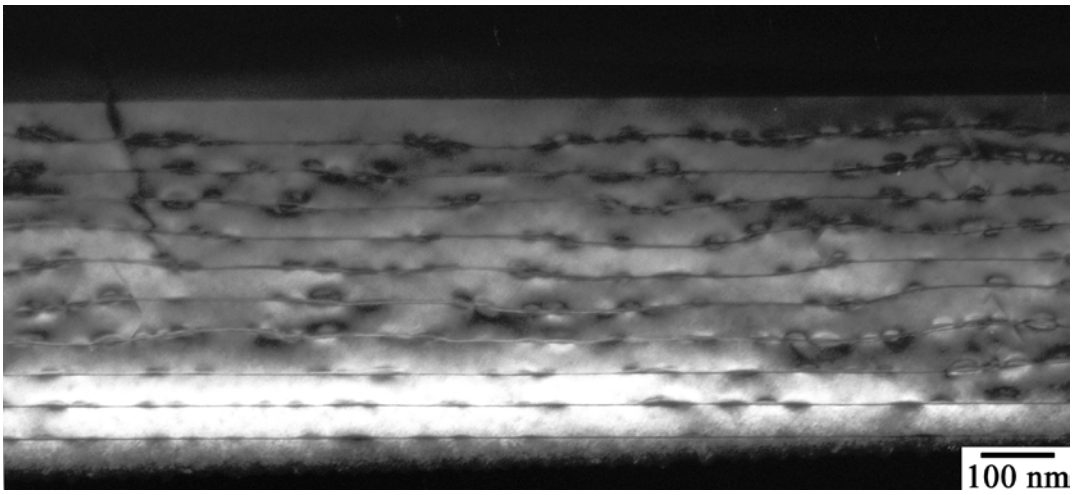

(a)

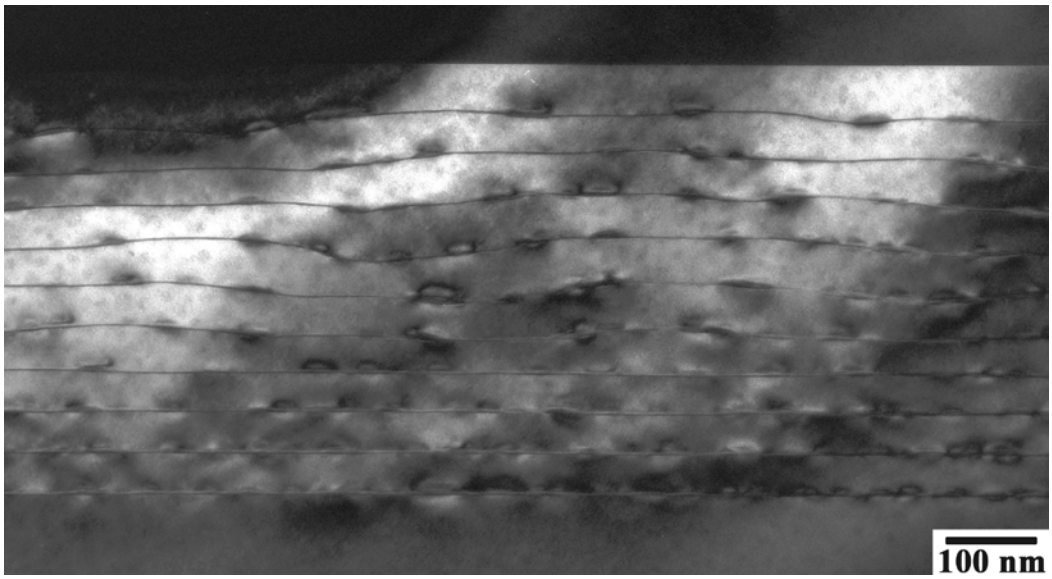

(b)

Figure 27. (200) Dark-field images of (a) sample 2050 and (b) sample 2399.

4.0 CONCLUSIONS

The major findings of the present study may be summarized as follows:

- Phase retrieval high-resolution transmission electron microscopy was used to investigate the role of interface tailoring in optimizing the properties of InAs/GaSb superlattices.
- The study shows that untalilored interfaces exhibit significant compositional grading in both cation and anion sublattices
- Interface tailoring leads to significant improvement in the compositional abruptness at the GaSb-on-InAs interface.
- The validity of this approach is demonstrated via image simulations performed on model structures with graded and abrupt interfaces, explicitly taking into account the role of interfacial strain.
- Detailed examination of InGaAs QDIP structures show that it is possible to achieve high quality multilayered stack with up to 20 layers. Optimization of growth parameters is however necessary to avoid dislocation generation during growth of the top GaAs contact layer.

5.0 REFERENCES

1. L. D. Nguyen, P. J. Tasker, and L. F. Eastman, IEEE Trans. Electron Devices **36**, 2243 (1989).

2. T. M. Cockermill, D. V. Forbes, J. A. Dantzig, and J. J. Coleman, IEEE J. Quantum Electron. **30**, 441 (1994).

3. F. Fuchs, U. Weimer, W. Pletschen, J. Schmitz, E. Ahlswede, M. Walther, J. Wagner, and P. Koidl, Appl. Phys. Lett. **71**, 3251 (1997).

4. G. W. Turner, H. K. Choi, and M. J. Manfra, Appl. Phys. Lett. **72**, 876 (1998).

5. X. Li, K. F. Longenbach, Y. Wang and W. I. Wang, IEEE Electron Device Lett. **13**, 192 (1992).

6. D. H. Chow, H. L. Dunlap, W. Williamson III, S. Enquist, B. K. Gilbert, S. Subramaniam, P. M. Lei, and G. H. Bernstein, IEEE Electron Device Lett. **17**, 69 (1996).

7. A. Ourmazd, D. W. Taylor, J. Cunningham and C. W. Tu, Phys. Rev. Lett. **62**, 933 (1989).

8. A. Ourmazd, F. H. Baumann, M. Bode, and Y. Kim, Ultramicroscopy **34**, 237 (1990).

9. S. Thoma and H. Cerva Ultramicroscopy **38**, 264 (1991).

10. A. Rosenauer, T. Remmele, D. Gerthsen, K. Tillman, and A. Forster, Optik **105**, 99 (1997).

11. A. Rosenauer and D. Gerthsen, Ultramicroscopy **76**, 49 (1999).

12. K.Mahalingam, “Stoichiometry of Interfaces in AlGaAs/GaAs Heterostructures grown by Molecular Beam Epitxay,” Air Force Research Laboratory Technical Report, Wright Patterson AFB, Task 99 (1998).

13. K.Mahalingam, “Transmission Electron Microscopy of III-V Heterostructures,” Air Force Research Laboratory Technical Report, Wright Patterson AFB, Task 150 (1999).

14. D. B. Williams and C. B. Carter, “Transmission Electron Microscopy,” Plenum Press, New York (1996).

15. K. Mahalingam, K. G. Eyink, G. J. Brown, D. L. Dorsey, C. F. Kisielowski and A. Thust, J. Microscopy, in press.

16. K. Mahalingam, K. G. Eyink, G. J. Brown, D. L. Dorsey, C. F. Kisielowski and A. Thust, Appl. Phys. Lett. **88**, 091904 (2006).

17. M. A. O'keefe, C. J. D. Hetherington, Y. C. Wang, E. C. Nelson, J. H. Turner, C. Kisielowski, J. O-Malm, R. Mueller, J. Ringnalda, M. Pan and A. Thust, Ultramicroscopy **89**, 215 (2001).

18. C. Kisielowski, C. J. D. Hetherington, Y. C. Wang, R. Kilaas, M. A. Okeefe and A. Thust, Ultramicroscopy **89**, 243 (2001).

19. *TrueImage* is a commercial software package distributed by FEI Inc, Portland, Oregon

20. W. M. J. Coene, A. Thust, M. Op de Beeck, and D. Van Dyck, Ultramicroscopy **64**, 109 (1996).

21. A. Thust, W. M. J. Coene, M. Op de Beeck, and D. Van Dyck, Ultramicroscopy **64**, 167 (1996).

22. R. Kilaas, J. Microscopy **190** 45 (1998).

23. L. A. Hemstreet, C.Y. Fong and J. S. Nelson, J. Vac. Sci. Technol. **B11**, 1693-1696 (1993).

24. M. M. J. Treacy and J. M. Gibson, J. Vac. Sci. Technol. **B4**, 1458-1466 (1986).

25. H. J. Haugan, G. J. Brown, F. Szmulowicz, L. Grazulis, W. C. Mitchel, S. Elhamri, W. D. Mitchell, J. Cryst. Growth **278**, 198 (2005).